

# Emergence and equilibration of jets in beta-plane turbulence

NAVID C. CONSTANTINOU\* AND PETROS J. IOANNOU

*Department of Physics, National and Kapodistrian University of Athens, Athens, Greece*

BRIAN F. FARRELL

*Department of Earth and Planetary Sciences, Harvard University, Cambridge, MA 02138*

(Submitted to the Journal of the Atmospheric Sciences)

## Abstract

Coherent large scale jets, not forced directly at the jet scale, are a prominent feature of rotating turbulence. These jets arise and are supported by systematic organization of the turbulent Reynolds stresses. Understanding the mechanism producing the required eddy momentum flux convergence, and how the jets and associated eddy field mutually adjust to maintain a steady jet structure at finite amplitude, constitute fundamental theoretical problems. Stochastic Structural Stability Theory (SSST) provides a framework for understanding the emergence and equilibration of jets based on a statistical mean state dynamics of turbulence closed at second order. SSST reveals a new manifold of turbulent equilibria and linearization of the SSST dynamics about these equilibria allows formulation of a structural stability theory that predicts the emergence of jets from homogeneous turbulence. We compare results for both formation and equilibration of turbulent jets made using the SSST closure with results of simulations made using quasi-linear and nonlinear models of barotropic turbulence on a beta-plane. SSST accurately predicts both the qualitative nature and in large measure the quantitative bifurcation structure associated with both the emergence and the finite amplitude equilibration of jets. Quantitative differences in some parameter values are traced to modification of the perturbation spectrum by perturbation-perturbation nonlinearity in the form of modification of the continuum or formation of discrete non-zonal structures. The reality of the manifold of these SSST jet structure modes is revealed by stochastic excitation of the stable counterparts of these predicted SSST modes in quasi-linear and nonlinear simulations. The resulting intermittent jets provide an explanation for the observations of latent jets.

## 1. Introduction

Spatially and temporally coherent jets are a common feature of turbulent flows in planetary atmospheres with the banded winds of the giant planets constituting a familiar example (Vasavada and Showman 2005). Fjørtoft (1953) noted that the essentially two dimensional large scale turbulence in planetary atmospheres, which results from the constraints of rapid rotation and strong stratification, would tend, given approximate conservation of energy and vorticity, to transfer turbulent energy to the largest scale available. This argument provides a conceptual basis for understanding the observed tendency for formation of large scale structure from small scale turbulence in planetary atmospheres. However, the observed large scale structure is dominated by zonal jets with specific form and, moreover, the scale of these jets is distinct from the largest scale in the flow. Rhines (1975) argued that

the observed jet scale results from the arrest of the inverse cascade at the length scale,  $\sqrt{u/\beta}$ , where  $\beta$  is the meridional gradient of planetary vorticity and  $u$  is the root mean square velocity in the turbulent fluid. In Rhines' interpretation this scale is identified with the scale at which the turbulent cascade is intercepted by the formation of propagating Rossby waves. More recently, it was proposed that jets in beta-plane turbulence arise from the tendency of turbulence to mix potential vorticity so that it becomes homogenized in limited regions forming potential vorticity staircases. The risers of these staircases correspond to thin prograde jets located at the latitudes of steep potential vorticity gradients separating parabolic retrograde jets corresponding to the well mixed steps of the staircase (Baldwin et al. 2007; Dritchel and McIntyre 2008). Alternatively, Miller (1990) and Robert and Sommeria (1991) associate large scale jets with structures of maximum entropy formed while respecting energy and vorticity conservation (Bouchet and Venaille 2012). Large scale structure in planetary flows has also been related to the

---

\* E-mail: [navidcon@phys.uoa.gr](mailto:navidcon@phys.uoa.gr)

existence of fixed points of the inviscid nonlinear planetary scale flow dynamics. Fixed point solutions were initially advanced to explain observations of large scale persistent structures in the atmosphere such as blocking (Charney and DeVore 1979; Legras and Ghil 1985). While fixed point structures are solutions to the large scale inviscid laminar flow dynamics the mechanism by which these large scale solutions arise and are maintained remains to be determined. SSST allows study of one mechanism of formation and maintenance of fixed point solutions through their interaction with the smaller scale turbulence (Bernstein 2009; Bernstein and Farrell 2010). Yet another proposed explanation for jet formation is modulational instability in which a zonal flow arises from nonlinear interaction of discrete Rossby waves (Gill 1974; Connaughton et al. 2010).

SSST provides an explanation for jet formation that is fundamentally based on the mutual interaction between jets and their associated field of turbulent eddies (Farrell and Ioannou 2003). SSST combines the full dynamics of the mean flow with the second order statistics of the turbulent field obtained from a stochastic turbulence model (STM) which has been shown to provide accurate eddy statistics for the atmosphere at large scale (Farrell and Ioannou 1993, 1994, 1995; Zhang and Held 1999; O’Gorman and Schneider 2007). These coupled equations determine the evolution of the mean zonal flow under the influence of its consistent field of eddies. In this theory, jets initially arise from a linear instability of this interaction and finite amplitude jets are identified as the nonlinear extension of these instabilities. The SSST instability of the stationary solutions as a function of parameters determines the bifurcation structure of the jet formation process. Srinivasan and Young (2012) developed a continuous formulation of SSST and used it to obtain analytic expressions for the emerging SSST instability in homogeneous beta-plane turbulence. A related quasi-linear approach to understanding finite amplitude turbulent equilibria in planetary atmospheres is the second order cumulant truncation method (CE2) (Marston et al. 2008; Marston 2012).

The quasi-linear (QL) approximation to the full nonlinear dynamics (NL) results when the perturbation-perturbation interactions are parametrized in the perturbation equations while interaction between the perturbations and the zonal mean flow is retained fully in the zonal mean equation. SSST is similar to QL with the additional assumption that the perturbation dynamics is that of the STM, which is equivalent to an infinite ensemble of perturbations, replacing the single realization evolved under QL. Because the SSST equations provide an autonomous and fluctuation-free dynamics of the statistical mean turbulent state, these equations facilitate analytic study of turbulent equilibria and their stability.

Previous studies demonstrated that unstable jets maintained by mean flow forcing can be equilibrated accurately using QL dynamics (Schoeberl and Lindzen 1984; DelSole

and Farrell 1996; Marston et al. 2008). In contrast to these studies, in this work we investigate the emergence and equilibration of jets from homogeneous turbulence in the absence of coherent external forcing at the jet scale. SSST predicts that infinitesimal perturbations with zonal jet form organize homogeneous turbulence to produce systematic upgradient fluxes giving rise to exponential jet growth and eventually to the establishment of finite amplitude equilibrium jets. Specifically, the SSST equations predict initial formation of jets by the most unstable eigenmode of the linearized SSST dynamics. The formation of zonal jets from initially homogeneous beta-plane turbulence was studied with the methods of SSST by Farrell and Ioannou (2003, 2007); Bakas and Ioannou (2011); Bakas and Ioannou (2013a), Srinivasan and Young (2012), Tobias and Marston (2013) and Parker and Krommes (2013). In agreement with SSST, Srinivasan and Young (2012) found that NL simulations exhibit jet emergence from a homogeneous turbulent state with subsequent establishment of finite amplitude jets. In this paper we use the full NL equations and their QL approximation together with SSST to examine further the mechanism of emergence and equilibration of jets from turbulence. We concentrate on the effects of perturbation-perturbation nonlinearity, which is not retained in QL or SSST, on jet bifurcation and equilibration.

## 2. Formulation of nonlinear barotropic dynamics on a beta-plane

Consider a beta-plane with  $x$  and  $y$  Cartesian coordinates along the zonal and the meridional direction respectively. The nondivergent zonal and meridional velocity fields are expressed in terms of a streamfunction,  $\psi$ , as  $u = -\partial_y \psi$  and  $v = \partial_x \psi$ . The vorticity on the beta-plane is  $q + 2\Omega + \beta y$ , where  $q \equiv \partial_x v - \partial_y u$  is the relative vorticity and  $2\Omega + \beta y$  is the planetary vorticity. The NL dynamics of this system is governed by the barotropic vorticity equation:

$$\partial_t q + u \partial_x q + v \partial_y q + \beta v = -r q - \nu_4 \Delta^2 q + \sqrt{\epsilon} F. \quad (1)$$

The flow is dissipated with linear damping at rate  $r$  and hyperviscosity with coefficient  $\nu_4$ . The term  $\Delta \equiv \partial_{xx}^2 + \partial_{yy}^2$  denotes the two-dimensional Laplacian. Periodic boundary conditions are imposed in  $x$  and  $y$  with periodicity  $2\pi L$ . In the above equation, distances have been nondimensionalized by a chosen length scale  $L$  and time by  $T = L/U$ , where  $U$  is a chosen velocity scale. We choose  $L = 5000$  km and  $U = 40$  m s<sup>-1</sup> for which the nondimensional time unit is  $T = 1.5$  day and the nondimensional terrestrial midlatitude value of  $\beta$  is 10. Turbulence is maintained by stochastic forcing. The spatial and temporal structure of the imposed forcing is specified by the function  $F(x, y, t)$ , while  $\epsilon$  controls the energy input rate by the forcing. This spatially and temporally homogeneous forcing will be specified later.

Velocity fields are decomposed into zonal-mean components (indicated upper case) and perturbations (indi-

cated lowercase and primes) so that the zonal velocity is  $U(y, t) + u'(x, y, t)$ , the meridional velocity is  $v'(x, y, t)$ , and the vorticity is  $Q(y, t) + q'(x, y, t)$ . Averaging in the zonal direction is denoted with a bar. Taking the zonal average of Eq. (1), we obtain two coupled equations for the evolution of the mean flow,  $U$ , and the associated perturbation field,  $q'$ :

$$\partial_t U = \overline{v'q'} - r_m U, \quad (2a)$$

$$\partial_t q' = -U \partial_x q' + (U_{yy} - \beta) \partial_x \psi' - r q' - \nu_4 \Delta^2 q' + F_e + \sqrt{\epsilon} F, \quad (2b)$$

where

$$F_e = \left[ \partial_y (\overline{v'q'}) - \partial_y (v'q') \right] - \partial_x (u'q') \quad (3)$$

is the nonlinear term representing the perturbation-perturbation interactions. In the above equation  $\psi' = \Delta^{-1} q'$ , where  $\Delta^{-1}$  is the inverse of the Laplacian. The mean flow and perturbation Eqs. (2) define the nonlinear system, NL. In Eqs. (2) the damping rates for the perturbation and mean flow,  $r$  and  $r_m$ , may differ. Hyperviscosity is included only in the perturbation equation for numerical stability. Stochastic forcing is applied only to the perturbation equations.

### 3. Formulation of quasi-linear barotropic dynamics on a beta-plane

The QL approximation of NL (Eqs. (2)) is obtained by parametrizing the perturbation-perturbation nonlinearity in Eq. (2b) as a state independent stochastic excitation and retaining the nonlinear Reynolds stress forcing,  $\overline{v'q'}$ , in the mean zonal flow equation to obtain the quasi-linear (QL) system:

$$\partial_t U = \overline{v'q'} - r_m U, \quad (4a)$$

$$\partial_t q' = -U \partial_x q' + (U_{yy} - \beta) \partial_x \psi' - r q' - \nu_4 \Delta^2 q' + \sqrt{\epsilon} F. \quad (4b)$$

The perturbation-perturbation nonlinearity,  $F_e$ , redistributes energy and enstrophy among the eddy scales. It can be shown that both the complete system (2) and its QL approximation (4) conserve both energy and enstrophy in the absence of forcing and dissipation.

Because in Eqs. (4)  $U$  is not a function of  $x$ , and the perturbation-perturbation nonlinearity has been neglected, the perturbation vorticity,  $q'$ , can be represented as a sum of non-interacting zonal harmonics,

$$q'(x, y, t) = \text{Re} \left[ \sum_{k=1}^{N_k} \hat{q}_k(y, t) e^{ikx} \right], \quad (5)$$

where  $\text{Re}$  denotes the real part and  $1, \dots, N_k$  are the zonal wavenumbers excited by the stochastic forcing in (4b). Because the channel is square with length  $2\pi$ , Fourier expansion

in the zonal or meridional direction assumes only integer wavenumber values. The structure of the stochastic forcing is expanded as:

$$F(x, y, t) = \text{Re} \left[ \sum_{k=1}^{N_k} \hat{F}_k(y, t) e^{ikx} \right]. \quad (6)$$

The stochastic forcing structure is assumed to have the form  $\hat{F}_k(y, t) = \sum_p F_{kp}(y) \xi_{kp}(t)$  so that it excites each of the  $F_{kp}(y)$  (to be specified) with coefficient  $\xi_{kp}(t)$ . The  $\xi_{kp}$  are temporally  $\delta$ -correlated and independently excite both the zonal harmonics and the meridional structures and are prescribed by:

$$\langle \xi_{kp}(t) \rangle = 0, \quad \langle \xi_{kp}(t) \xi_{mn}^*(t') \rangle = \delta_{km} \delta_{pn} \delta(t - t'), \quad (7)$$

where the angle bracket denotes an ensemble average over realizations.

The two-point perturbation vorticity covariance is defined as:

$$C(x_a, y_a, x_b, y_b, t) = \langle q'(x_a, y_a, t) q'(x_b, y_b, t) \rangle. \quad (8)$$

Because of the independence of the excitations,  $\xi_{k\ell}$ , and the separability of the linear dynamics (4b) in  $x$ , the covariance is homogeneous in the zonal direction at all times and can be expanded in the difference coordinate,  $x_a - x_b$ , as:

$$\begin{aligned} C(x_a - x_b, y_a, y_b, t) &= \\ &= \frac{1}{2} \text{Re} \left[ \sum_{k=1}^{N_k} \langle \hat{q}_k(y_a, t) \hat{q}_k^*(y_b, t) \rangle e^{ik(x_a - x_b)} \right] \\ &= \frac{1}{2} \text{Re} \left[ \sum_{k=1}^{N_k} \hat{C}_k(y_a, y_b, t) e^{ik(x_a - x_b)} \right], \end{aligned} \quad (9)$$

where  $\hat{C}_k(y_a, y_b, t)$  is the latitudinal covariance of the vorticity field at zonal wavenumber  $k$  and time  $t$ .

The spatial covariance of the forcing is defined as

$$Q(x_a, x_b, y_a, y_b) = \langle F(x_a, y_a, t) F(x_b, y_b, t) \rangle, \quad (10)$$

and is assumed to be homogeneous in both  $x$  and  $y$ , which means that it depends only in the difference coordinates of the two points,  $x_a - x_b$  and  $y_a - y_b$ , and therefore has Fourier expansion:

$$\begin{aligned} Q(x_a - x_b, y_a - y_b) &= \\ &= \text{Re} \left\{ \sum_{k=1}^{N_k} \sum_{\ell=-\infty}^{+\infty} \hat{Q}_{k\ell} e^{i[k(x_a - x_b) + \ell(y_a - y_b)]} \right\}. \end{aligned} \quad (11)$$

At zonal wavenumber  $k$ , the corresponding latitudinal spatial covariance is:

$$\hat{Q}_k(y_a - y_b) = \sum_{\ell=-\infty}^{+\infty} \hat{Q}_{k\ell} e^{i\ell(y_a - y_b)}. \quad (12)$$

Fourier coefficients of the forcing covariance, for only positive values of zonal wavenumbers,  $k$ , (cf. Eq. (11)) can be related to Fourier expansions in both positive and negative zonal wavenumbers,

$$Q(x_a - x_b, y_a - y_b) = \sum_{\substack{k=-\infty \\ k \neq 0}}^{+\infty} \sum_{\ell=-\infty}^{+\infty} \tilde{Q}_{k\ell} e^{i[k(x_a - x_b) + \ell(y_a - y_b)]}, \quad (13)$$

through:

$$\tilde{Q}_{k,\ell} = \frac{\hat{Q}_{k,\ell}}{2}, \quad \tilde{Q}_{-k,\ell} = \frac{\hat{Q}_{k,-\ell}}{2} \quad \text{for } k > 0. \quad (14)$$

For the derivation of Eq. (14) the use of the symmetry of the forcing covariance under exchange of the two points is used.

#### 4. Formulation of SSST barotropic dynamics on a beta-plane

Taking the Fourier transform of Eq. (4b) and discretizing the fields on a meridional grid we obtain the corresponding matrix form:

$$\partial_t \hat{\mathbf{q}}_k = \mathbf{A}_k(\mathbf{U}) \hat{\mathbf{q}}_k + \sqrt{\epsilon} \hat{\mathbf{F}}_k, \quad (15)$$

with

$$\mathbf{A}_k(\mathbf{U}) = -ik [\mathbf{U} - (\mathbf{U}_{yy} - \beta \mathbf{I}) \mathbf{\Delta}_k^{-1}] - r \mathbf{I} - \nu_4 \mathbf{\Delta}_k^2. \quad (16)$$

The state,  $\hat{\mathbf{q}}_k$ ; the zonal mean flow,  $\mathbf{U}$ ; and the Fourier coefficient of the forcing,  $\hat{\mathbf{F}}_k$ ; are column vectors with elements the values at the  $N_y$  discretization points,  $y_p$ ,  $p = 1, \dots, N_y$ . In the matrix  $\mathbf{A}_k$ ,  $\mathbf{\Delta}_k = \mathbf{D}^2 - k^2 \mathbf{I}$ , with  $\mathbf{D}^2$  the discretized  $\partial_{yy}$  operator,  $\mathbf{I}$  the identity matrix,  $\mathbf{\Delta}_k^{-1}$  the inverse of  $\mathbf{\Delta}_k$ ,  $\mathbf{U}$  the diagonal matrix with diagonal elements  $\mathbf{U}$ , and  $\mathbf{U}_{yy}$  the diagonal matrix with diagonal elements  $\mathbf{D}^2 \mathbf{U}$ . With this discretization the latitudinal covariance  $\hat{C}_k(y_a, y_b, t)$  of Eq. (9) becomes the matrix  $\mathbf{C}_k = \langle \hat{\mathbf{q}}_k \hat{\mathbf{q}}_k^\dagger \rangle$ , with  $\dagger$  denoting the Hermitian transpose.

With  $N_y$  discretization points in  $y$ , the forcing structure,  $\hat{\mathbf{F}}_k$ , is specified by a  $N_y \times N_y$  matrix  $\mathbf{F}_k$ , so that for each  $k$  the white noise process  $\xi_{kp}$  excites the spatial structure given by the  $p$ -th column of  $\mathbf{F}_k$ . Therefore the forcing of the  $k$ -th wavenumber is written as:

$$[\hat{\mathbf{F}}_k]_j = \sum_{p=1}^{N_y} [\mathbf{F}_k]_{jp} \xi_{kp}(t). \quad (17)$$

The forcing structure matrices,  $\mathbf{F}_k$ , are normalized, as will be described in section 5.

The ensemble average of the covariance of the perturbations in Eq. (15),  $\mathbf{C}_k$ , satisfies the time dependent Lyapunov equation:

$$\partial_t \mathbf{C}_k = \mathbf{A}_k(\mathbf{U}) \mathbf{C}_k + \mathbf{C}_k \mathbf{A}_k(\mathbf{U})^\dagger + \epsilon \mathbf{Q}_k, \quad (18)$$

as in Farrell and Ioannou (1996). The overall forcing amplitude is controlled by the square root of the energy input rate,  $\epsilon$ , and the spatial covariance of the forcing enters this equation as  $\mathbf{Q}_k = \mathbf{F}_k \mathbf{F}_k^\dagger$ , or equivalently in terms of the spectral coefficients of the forcing covariance,  $\hat{Q}_{k\ell}$  (cf. Eq. (11)), as:

$$[\mathbf{Q}_k]_{bd} = \sum_{\ell=-N_y/2}^{N_y/2-1} \hat{Q}_{k\ell} e^{i\ell(y_b - y_d)}. \quad (19)$$

The summation extends over meridional wavenumbers  $-N_y/2$  and  $N_y/2 - 1$  because only these wavenumbers are resolved when  $N_y$  points in the meridional direction are retained (for  $N_y$  even).

The covariances,  $\mathbf{C}_k$ , determine the second order statistics of all perturbation fields. For example, the ensemble average of the vorticity flux,

$$\langle v'q' \rangle = \sum_{k=1}^{N_k} \frac{1}{2} \text{Re} \left( \langle \hat{v}_k \hat{q}_k^* \rangle \right), \quad (20)$$

is expressed in terms of the covariances,  $\mathbf{C}_k$ , as:

$$\begin{aligned} \mathbf{vq} &= - \sum_{k=1}^{N_k} \frac{k}{2} \text{vecd} \left[ \text{Im} \left( \langle \mathbf{\Delta}_k^{-1} \hat{\mathbf{q}}_k \hat{\mathbf{q}}_k^\dagger \rangle \right) \right] \\ &= - \sum_{k=1}^{N_k} \frac{k}{2} \text{vecd} \left[ \text{Im} (\mathbf{\Delta}_k^{-1} \mathbf{C}_k) \right], \end{aligned} \quad (21)$$

where  $\mathbf{vq}$  is the column vector of the values of  $\langle v'q' \rangle$  and  $\text{Im}$  denotes the imaginary part. We denote with  $\text{vecd}(\mathbf{M})$  the column vector consisting of the diagonal elements of matrix  $\mathbf{M}$ .

Under the ergodic assumption that the zonal average of the perturbation covariance can be obtained from the ensemble average, we substitute  $\overline{v'q'} = \langle v'q' \rangle$  in Eq. (4a) to obtain an equation for the evolution of the zonal mean flow, which is linear in the  $\mathbf{C}_k$ :

$$\partial_t \mathbf{U} = - \sum_{k=1}^{N_k} \frac{k}{2} \text{vecd} \left[ \text{Im} (\mathbf{\Delta}_k^{-1} \mathbf{C}_k) \right] - r_m \mathbf{U}. \quad (22)$$

The system of equations formed by (18) and (22), define the SSST dynamics for the evolution of the zonally averaged flow,  $\mathbf{U}$ , and its associated ensemble average perturbation covariances,  $\mathbf{C}_k$ :

$$\partial_t \mathbf{U} = - \sum_{k=1}^{N_k} \frac{k}{2} \text{vecd} \left[ \text{Im} (\mathbf{\Delta}_k^{-1} \mathbf{C}_k) \right] - r_m \mathbf{U}, \quad (23a)$$

$$\partial_t \mathbf{C}_k = \mathbf{A}_k(\mathbf{U}) \mathbf{C}_k + \mathbf{C}_k \mathbf{A}_k(\mathbf{U})^\dagger + \epsilon \mathbf{Q}_k. \quad (23b)$$



## 5. Specification of the stochastic forcing structure

Because the SSST instability mechanism differs for the case of isotropic and non-isotropic forcing we consider examples of both forcing structures, in order to investigate the influence of turbulence symmetry on the SSST instability. The jet forming instability in the presence of homogeneous, non-isotropic forcing arises from the upgradient fluxes induced by the shearing of the turbulence by the infinitesimal jet, while the upgradient fluxes for isotropic forcing arise from the refraction of the eddies caused by the variation in the potential vorticity gradient induced by the infinitesimal jet (Bakas and Ioannou 2013a).

Three stochastic forcing structures will be used in our investigation of the correspondence of SSST, QL and NL dynamics. The first independently excites a set of zonal wavenumbers. This forcing was first used by Williams (1978) to parametrize excitation of barotropic dynamics by baroclinic instabilities. This method of forcing was also used by DelSole (2001) in his study of upper-level tropospheric jet dynamics and in the study of jet formation using SSST dynamics by Farrell and Ioannou (2003, 2007) and Bakas and Ioannou (2011). This stochastic forcing is spatially homogeneous but not isotropic and will be denoted as NIF (non-isotropic forcing). The second is an isotropic ring forcing (denoted IRF) concentrated near a single total wavenumber. This forcing structure has been used extensively in studies of beta-plane turbulence (cf. Vallis and Maltrud 1993) and had also been used in the recent study of Srinivasan and Young (2012). It was introduced by Lilly (1969), in order to isolate the inverse cascade from the forcing in a study of two dimensional turbulence. The third is an isotropic ring forcing, similar to the second, but with the forcing distributed over a wider annular region around the central wavenumber.

Recall that the stochastic forcing,

$$F(x_i, y_j, t) = \text{Re} \left[ \sum_{k=1}^{N_k} \sum_{p=1}^{N_y} [\mathbf{F}_k]_{jp} \xi_{kp}(t) e^{ikx_i} \right], \quad (24)$$

is correlated in  $y$  by the columns of the matrix  $\mathbf{F}_k$ . For the non-isotropic forcing (NIF) this meridional structure of the forcing correlation, in a periodic channel with period  $2\pi$  in  $y$ , is specified by:

$$[\mathbf{F}_k]_{jp} = c_k \left[ e^{-(y_j - y_p)^2 / (2s^2)} + e^{-(y_j - 2\pi - y_p)^2 / (2s^2)} + e^{-(y_j + 2\pi - y_p)^2 / (2s^2)} \right]. \quad (25)$$

Each forcing is gaussian correlated in  $y$ , with half-width  $s = 0.2/\sqrt{2}$  and zonal waves  $k = 1, \dots, 14$  are forced. Because the stochastic forcing is  $\delta$ -correlated in time, the energy input rate does not depend on the state and can be independently specified (cf. Appendix B). The normalization constant,  $c_k$ ,

in (25) is chosen so that each  $k$  is excited equally and one unit of energy is injected in total, so that  $\epsilon$  is the total energy input rate in the NL, QL or SSST simulations.

The isotropic ring forcing is specified by:

$$[\mathbf{F}_k]_{jp} = c w_{kp}(K) e^{i\ell(p) y_j}, \quad (26)$$

with  $\ell(p) = (p - 1) - N_y/2$  and  $K = \sqrt{k^2 + \ell^2}$ . The first isotropic forcing (IRFh, h refers to the “hat-like” distribution in wavenumber space) is specified by

$$w_{kp} = \begin{cases} 1 & , \quad |K - K_f| \leq \delta k_f, \\ 0 & , \quad |K - K_f| > \delta k_f. \end{cases} \quad (27)$$

For IRFh we choose  $K_f = 14$  and  $\delta k_f = 1$ . The second isotropic forcing (IRFg, g refers to Gaussian distribution in wavenumber space) is specified by:

$$w_{kp} = c \exp \left[ -\frac{(K - K_f)^2}{2 \delta k_f^2} \right]. \quad (28)$$

For IRFg we choose  $K_f = 14$  and  $\delta k_f = 8/\sqrt{2}$ . The normalization constant,  $c$ , is chosen for both cases so that the total energy input rate is unity (cf. Appendix B). IRFh and IRFg are both spatially homogeneous and nearly isotropic in a finite doubly periodic domain. They approach exact isotropy as the domain size increases.

Plots of the corresponding power spectra together with instantaneous realizations of the stochastic forcing both in vorticity and streamfunction are shown in Fig. 1 for the three types of forcing structures. The thin IRFh ring forcing primarily excites vortices of scale  $1/K_f$  in the flow that are evident in both the vorticity and streamfunction fields, while IRFg produces a streamfunction field dominated by large scale structure.

## 6. Stability of the SSST homogeneous equilibrium state

Because of the homogeneity of the stochastic forcing,  $\mathbf{v}\mathbf{q} = 0$  in the absence of symmetry breaking by a mean flow and the SSST equations admit the homogeneous equilibrium solution:

$$\mathbf{U}^E = 0, \quad \mathbf{C}^E = \sum_{k=1}^{N_k} \mathbf{C}_k^E \quad \text{with} \quad \mathbf{C}_k^E = \frac{\epsilon}{2r} \mathbf{Q}_k, \quad (29)$$

for  $\nu_4 = 0$ . The spatial covariance of the perturbation field in this equilibrium state without jets is identical to the spatial covariance of the stochastic forcing. The stability of this equilibrium state,  $(\mathbf{U}^E, \mathbf{C}^E)$ , to jet formation is determined by the linear dynamics of the evolution of perturbations  $(\delta\mathbf{U}, \delta\mathbf{C}_1, \dots, \delta\mathbf{C}_{N_k})$  to this equilibrium. These perturba-

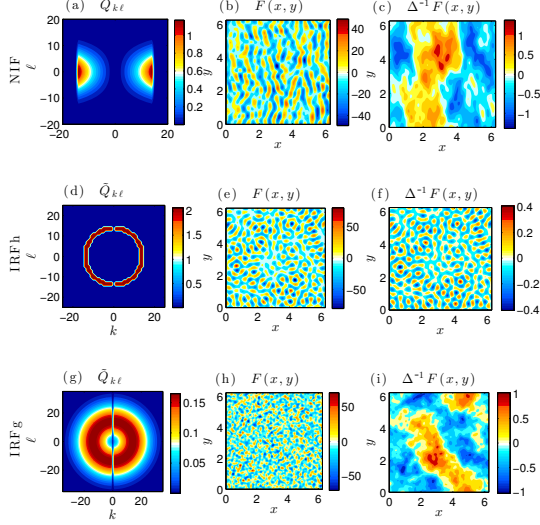


**Figure 1:** Stochastic forcing spatial wavenumber spectra and examples of realizations in physical variables. Shown for NIF with zonal wavenumbers  $k = 1, \dots, 14$  and  $s = 0.2/\sqrt{2}$  are: (a) entrophy spectrum,  $\tilde{Q}_{k\ell}$ , (b) vorticity, (c) streamfunction. For IRFh at  $K_f = 14$  and  $\delta k_f = 1$ : (d) entrophy spectrum  $\tilde{Q}_{k\ell}$ , (e) vorticity, (f) streamfunction. For IRFg at  $K_f = 14$  and  $\delta k_f = 8/\sqrt{2}$ : (g) entrophy spectrum  $\tilde{Q}_{k\ell}$ , (h) vorticity, (i) streamfunction.

tions satisfy the linear equations:

$$\partial_t \delta \mathbf{U} = - \sum_{k=1}^{N_k} \frac{k}{2} \text{vecd} \left[ \text{Im}(\Delta_k^{-1} \delta \mathbf{C}_k) \right] - r_m \delta \mathbf{U}, \quad (30a)$$

$$\partial_t \delta \mathbf{C}_k = \mathbf{A}_k^E \delta \mathbf{C}_k + \delta \mathbf{C}_k \left( \mathbf{A}_k^E \right)^\dagger + \delta \mathbf{A}_k \mathbf{C}_k^E + \mathbf{C}_k^E (\delta \mathbf{A}_k)^\dagger, \quad (30b)$$

which are obtained by linearizing the SSST system (23) about  $(\mathbf{U}^E, \mathbf{C}^E)$ . In the above equations  $\mathbf{A}_k^E \equiv \mathbf{A}_k(\mathbf{U}^E)$  is the operator linearized about the equilibrium mean zonal flow,  $\mathbf{U}^E$ , and  $\delta \mathbf{A}_k$  is  $\delta \mathbf{A}_k = -ik [\delta \mathbf{U} - (\delta \mathbf{U})_{yy} \Delta_k^{-1}]$ .

The eigenfunctions and eigenvalues of Eqs. (30) are readily obtained in the case of the homogeneous equilibrium state (29). The mean flow part of these eigenfunctions are found to consist of  $n$  pairs of alternating prograde and retrograde jets. Details on the method of determination of the eigenvalues can be found in Appendix C.

We now investigate the stability of the homogeneous equilibrium state (29) as a function of the energy input rate,  $\epsilon$ . In the absence of forcing,  $\epsilon = 0$ , it can be easily verified that the eigenvalues are either  $\sigma = -2r$  (corresponding to eigenfunctions with  $\delta \mathbf{U} = 0$ ) or  $\sigma = -r_m$  (corresponding to eigenfunctions with all  $\delta \mathbf{C}_k = 0$ ) and the zero equilibrium state is clearly stable. In the presence of forcing the mean zonal flow perturbations are coupled to the perturbation

covariance and this coupling may give rise to an SSST instability. We will demonstrate that such a structural instability occurs for energy input rate  $\epsilon > \epsilon_c$ , resulting in transition to an inhomogeneous equilibrium with finite amplitude zonal jets.

Growth rates,  $\sigma_r = \text{Re}(\sigma)$ , as a function of the meridional wavenumber of the mean zonal flow perturbation,  $n$ , and of the energy input rate,  $\epsilon$ , are shown in Fig. 2 for a case with NIF and similarly for IRFh in Fig. 3. For both types of forcing, instability occurs for  $\epsilon > \epsilon_c$  over a band of mean zonal flow wavenumbers,  $n$ . In all cases the  $\sigma(n)$  associated with the largest growth rate has zero imaginary part.

Growth rate curves are shown in Fig. 4 for various forcings and damping amplitudes. In the next section the predictions of this SSST stability analysis will be compared with the corresponding QL and NL simulations. While QL and NL simulations reveal the bifurcation, they do not provide theoretical predictions for the bifurcation structure of turbulent equilibria. We wish to examine the circumstances under which the underlying bifurcation structure predicted theoretically by the SSST eigenfunctions is reflected in the QL and NL realizations.

## 7. Bifurcations predicted by SSST and their reflection in QL and NL simulations

We examine the approximate counterpart in NL and QL simulations of the SSST structural instability by comparing the evolution of the domain averaged energy of the zonal flow:

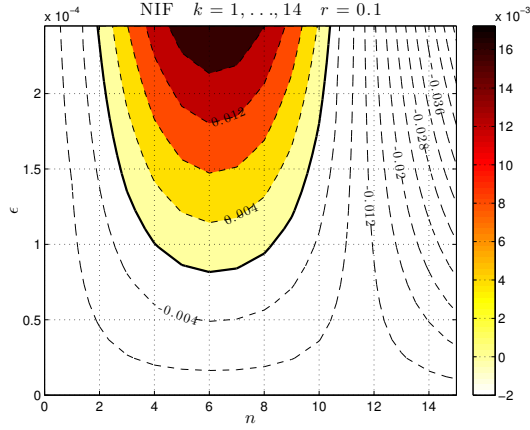
$$E_m(t) = \frac{1}{L_x L_y} \iint \frac{1}{2} U^2 dx dy. \quad (31)$$

The amplitude of the zonal flow is measured with the zonal mean flow index (zmf) defined as  $\text{zmf} = E_m/(E_m + E_p)$ , where  $E_m$  is the time averaged energy of the zonal mean flow, given in Eq. (31), and  $E_p$  is the time average of the domain averaged kinetic energy of the perturbations,

$$E_p(t) = \frac{1}{L_x L_y} \iint \frac{1}{2} (u'^2 + v'^2) dx dy. \quad (32)$$

### a. Correspondence of jet emergence in NL, QL and SSST for moderate damping

The case of NIF with  $r = 0.1$ ,  $r_m = 0.01$  and  $\epsilon = 1.5\epsilon_c$  is plotted in Fig. 5. For this forcing and parameters, SSST predicts that maximum growth occurs for the sinusoidal zonal mean flow perturbation with  $n = 6$ , as seen in Fig. 4a. Introduction of this eigenfunction in the SSST dynamics produces initially the predicted exponential growth, followed by approach to an equilibrium consisting of 6 finite amplitude jets. This equilibration demonstrates that the SSST dynamics includes the mechanism both of the instability and of the finite amplitude stabilization of the jet formation instability. Corresponding simulations with the QL and NL dynamics using the same parameters for the damping and



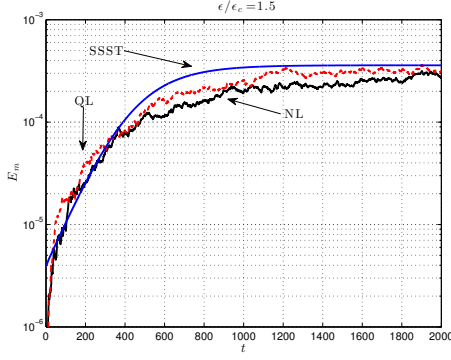


**Figure 5:** Development of mean flow energy,  $E_m$ , for NL and QL simulations starting from a state of rest with NIF at  $k = 1, \dots, 14$  and  $\epsilon = 1.5\epsilon_c$ . Also shown is the exponential growth and subsequent equilibration of  $E_m$  under SSST dynamics with initial condition the most unstable SSST eigenfunction. This figure demonstrates that SSST dynamics accurately predicts nonlinear jet equilibration at finite amplitude as well as the initial instability and exponential growth of the jets. Parameters are  $\beta = 10$ ,  $r = 0.1$ ,  $r_m = 0.01$ .

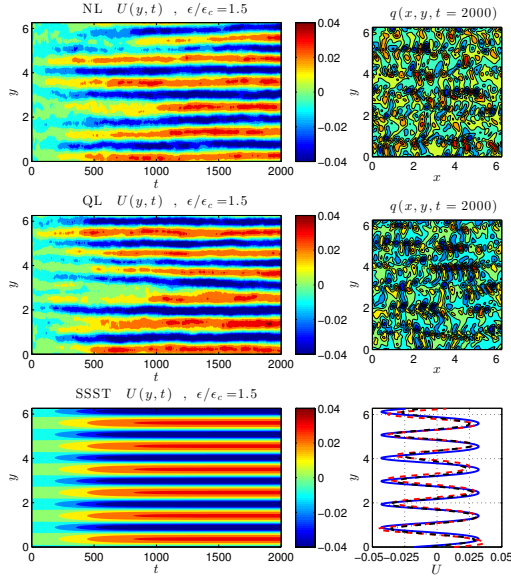


**Figure 6:** Hovmöller diagrams of jet emergence in the NL, QL and SSST simulations shown in Fig. 5. Shown for the NL, QL and SSST simulations are  $U(y, t)$  (left panels) and for the NL and QL simulations the vorticity fields at  $t = 2000$  (top and middle right panels). Also shown are the equilibrium jets in the NL (dash-dot-black), QL (dashed - red), and SSST (solid - blue) simulation (bottom right panel). This figure shows that SSST predicts the structure, growth and equilibration of weakly forced jets in both the QL and NL simulations (cf. Fig. 4a).

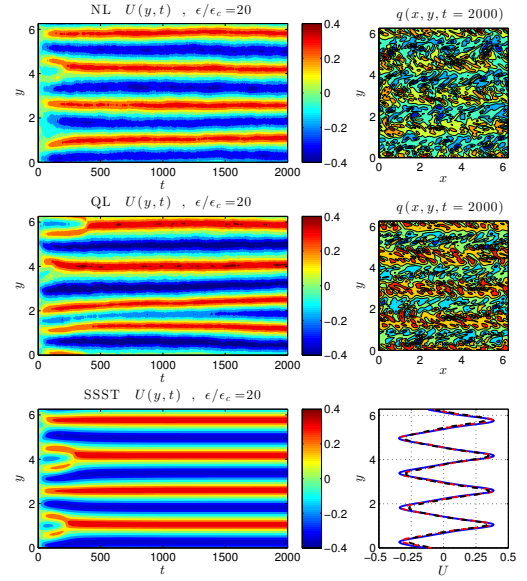


**Figure 7:** Hovmöller diagrams of jet emergence in NL, QL and SSST simulations with NIF forcing of  $k = 1, \dots, 14$  with  $\epsilon = 20\epsilon_c$ . Shown for the NL, QL and SSST simulations are  $U(y, t)$  (left panels) and for the NL and QL simulations the vorticity fields at  $t = 2000$  (top and middle right panels). Also shown are the equilibrium jets in the NL (dash-dot-black), QL (dashed - red), and SSST (solid - blue) simulation (bottom right panel). This figure shows that SSST predicts the structure, growth and equilibration of immoderately forced jets in both the QL and NL simulations (cf. Fig. 4b). Parameters are  $r = 0.1$ ,  $r_m = 0.01$  and  $\beta = 10$ .

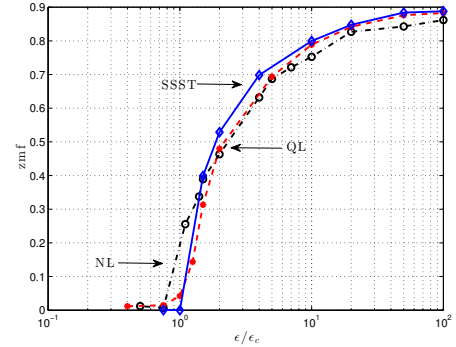


**Figure 8:** Bifurcation structure comparison for jet formation in SSST, QL, and NL. Shown is the zmf index of jet equilibria for NIF at  $k = 1, \dots, 14$  as a function of the forcing amplitude  $\epsilon/\epsilon_c$  for the NL simulation (dash-dot and circles), the QL simulation (dashed and dots) and the SSST (solid and diamonds). Parameters are  $\beta = 10$ ,  $r = 0.1$ ,  $r_m = 0.01$ .



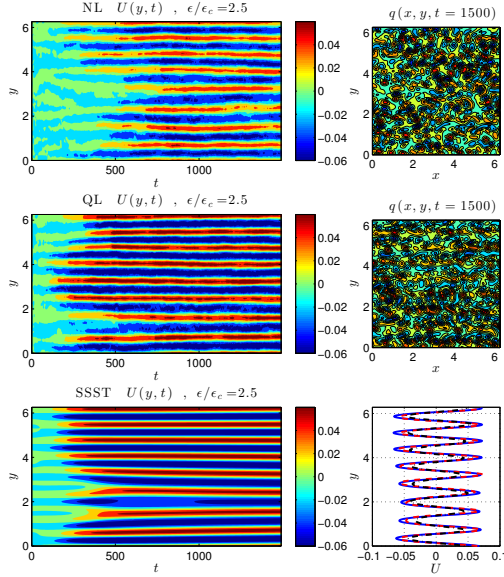


**Figure 9:** Hovmöller diagrams of jet emergence in NL, QL and SSST simulations with IRFh forcing at  $\epsilon = 2.5\epsilon_c$  and with  $K_f = 14$ ,  $\delta k_f = 1$ . Shown for the NL, QL and SSST simulations are  $U(y, t)$  (left panels) and for the NL and QL simulations the vorticity fields at  $t = 1500$  (top and middle right panels). Also shown are the equilibrium jets in the NL (dash-dot-black), QL (dashed - red), and SSST (solid - blue) simulation (bottom right panel). This figure shows that SSST predicts the structure, growth and equilibration of jets obtained in both the QL and NL simulations (cf. Fig. 4c). Parameters are  $r = 0.1$ ,  $r_m = 0.01$  and  $\beta = 10$ .

bifurcation structure is paralleled by the QL and NL simulations over a wide range of forcing amplitudes. It also demonstrates that both the NL and QL simulations equilibrate at finite amplitude with nearly the same structure as the SSST equilibria.

Similar agreement is obtained with IRFh at  $K_f = 14$  with  $\delta k_f = 1$  and damping parameters  $r = 0.1$ ,  $r_m = 0.01$  for which the case with  $\epsilon = 2.5\epsilon_c$  is shown in Fig. 9. Maximum growth in this case occurs at zonal wavenumber  $n = 8$  (cf. Fig. 4c) and again the SSST predictions for both initiation of the instability and its saturation are reflected in the QL and NL simulations. The bifurcation diagram for this IRFh forcing and damping is plotted in Fig. 10. For this case also the critical value,  $\epsilon_c$ , is correctly predicted by SSST stability analysis, but for supercritical forcing amplitudes the zonal flow predicted by SSST and QL is stronger and the perturbation energy smaller than the corresponding zonal flow and perturbation energy obtained in the NL simulations. This difference between the NL and both the SSST predictions and QL simulations at high levels of forcing, corresponding to high supercriticality, is only in part accounted for by the spreading of the spectrum in NL as shown by the SSSTb response in Fig. 10. The major part of this difference

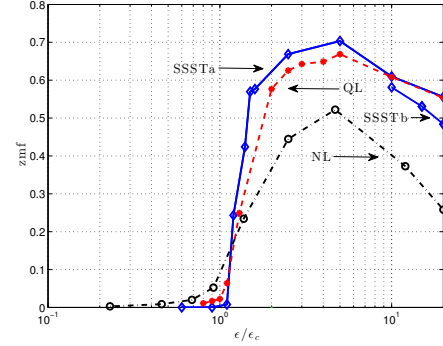


**Figure 10:** Bifurcation structure comparison for jet formation in SSST, QL, and NL. Shown is the zmf index of jet equilibria for IRFh with  $K_f = 14$  and  $\delta k_f = 1$  as a function of the energy input rate  $\epsilon/\epsilon_c$  for the NL simulation (dash-dot and circles), the QL simulation (dashed and dots) and the SSST (solid and diamonds) for IRFh (SSSTa), as well as the SSST for the equivalent spectrum to that obtained in NL as a consequence of modification of the IRFh spectrum by the nonlinear cascade (SSSTb) with energy input rate  $\epsilon = 20\epsilon_c$ . This figure shows that the bifurcation to jet formation in NL and QL simulations is captured by SSST and that SSST overestimates the NL jet amplitude when the forcing is high, even when account is taken for the nonlinear modification of the spectrum. Parameters are  $\beta = 10$ ,  $r = 0.1$ ,  $r_m = 0.01$ .

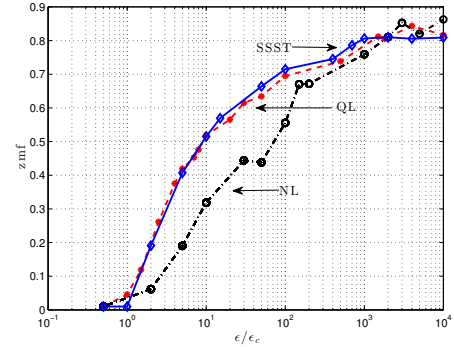


**Figure 11:** Bifurcation structure comparison for jet formation in SSST, QL, and NL. Shown is the zmf index of jet equilibria for IRFg with  $K_f = 14$  and  $\delta k_f = 8/\sqrt{2}$  as a function of the energy input rate  $\epsilon/\epsilon_c$  for the NL simulation (dash-dot and circles), the QL simulation (dashed and dots) and the SSST (solid and diamonds). Parameters are  $\beta = 10$ ,  $r = 0.1$ ,  $r_m = 0.01$ .



is due to the nonlinear perturbation-perturbation interactions in NL that disrupt the upgradient momentum transfer. This disruption is accentuated by the peculiar efficiency with which the narrow ring forcing, IRFh, gives rise to vortices as can be seen in Fig. 1d-f. We verify that this narrow ring forcing is responsible for depressing NL equilibrium jet strength at high supercriticality by broadening the forcing distribution in the form of IRFg for which  $K_f = 14$  and  $\delta k_f = 8/\sqrt{2}$  (cf. Fig. 1). Using this modified forcing and other parameters as in Fig. 10, we obtain agreement between SSST, QL and NL simulations, as is shown in Fig. 11.

*b. Correspondence of jet emergence in NL, QL and SSST for weak damping*

For sufficiently small perturbation damping,  $r$ , the SSST critical energy input rate,  $\epsilon_c$ , for jet emergence differs from the critical energy input rate,  $\epsilon_c^{(NL)}$ , at which finite amplitude and persistent zonal mean flows form in the NL simulations. For example, for perturbation damping  $r = 0.01$ ,  $r_m = 0.01$  the NL simulations bifurcate at  $\epsilon_c^{(NL)} \approx 11\epsilon_c$  under NIF forcing with  $k = 1, \dots, 14$  and at  $\epsilon_c^{(NL)} \approx 4\epsilon_c$  under IRFh forcing at  $K_f = 14$  and  $\delta k_f = 1$ . The bifurcation diagram for the NIF forcing is shown in Fig. 12 and for the IRFh forcing in Fig. 13. Similar behavior was noted by Srinivasan and Young (2012). The reason for the difference in the NL and SSST bifurcation curves will be explained in section 8. Typical structure of the emerging jets for the IRFh forcing at these parameters is shown in Fig. 14.

## 8. Development of the turbulence spectra in non-linear simulations and its influence on SSST stability

Both QL and SSST dynamics exclude interactions among perturbations and include only the non-local interactions between zonally averaged quantities, with  $k = 0$ , and perturbations, with  $k \neq 0$ . Therefore, there is no enstrophy or energy cascade in wavenumber space in either QL or SSST dynamics and the equilibrium state in SSST ( $\mathbf{U}^E = 0$  and  $\mathbf{C}^E = \epsilon \sum_{k=1}^{N_k} \mathbf{Q}_k / 2r$ ) has a spectrum proportional to the spectrum of the forcing, which is fully determined by the forcing covariances,  $\mathbf{Q}_k$ . However, this is not true in NL dynamics which includes perturbation-perturbation interactions producing enstrophy/energy cascades. For example, in NL an isotropic ring forcing is distorted as time progresses by the nonlinear perturbation-perturbation interactions becoming concentrated at lower wavenumbers and forming the characteristic dumbbell shape seen in beta-plane turbulence simulations (Vallis and Maltrud 1993), as shown in Fig. 15. While the primary dynamical observation to be made from the similarity of the jet bifurcation structure in SSST, QL, and NL is that perturbation-perturbation nonlinearity mediated turbulent cascades are not responsible for jet formation, still it is to be expected that the statistical equilibrium state

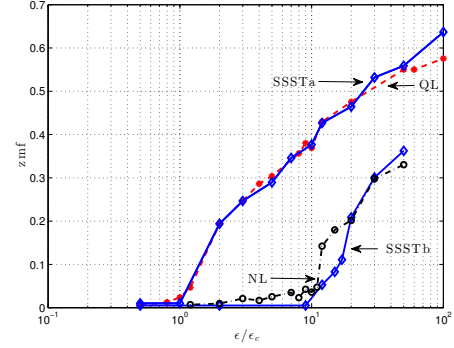


**Figure 12:** Bifurcation structure comparison for jet formation in SSST, QL, and NL. Shown is the zmf index of jet equilibria for NIF at  $k = 1, \dots, 14$  as a function of the forcing amplitude  $\epsilon/\epsilon_c$  for the NL simulation (dash-dot and circles), the QL simulation (dashed and dots) and the SSST NIF (SSSTa), as well as the SSST for the equivalent spectrum to that obtained in NL as a consequence of modification of the NIF spectrum by the nonlinear cascade (SSSTb). The bifurcation in the NL simulations occurs at  $\epsilon_c^{(NL)} \approx 11\epsilon_c$ . This figure shows that the structure of the jet in NL simulations is captured by the SSST if account is taken of the nonlinear modification of the spectrum. Parameters are  $\beta = 10$ ,  $r = 0.01$ ,  $r_m = 0.01$ .

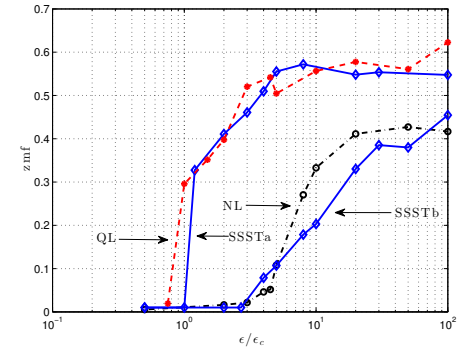


**Figure 13:** Bifurcation structure comparison for jet formation in SSST, QL, and NL. Shown is the zmf index of jet equilibria for IRFh at  $K_f = 14$  with  $\delta k_f = 1$  as a function of the forcing amplitude  $\epsilon/\epsilon_c$  for the NL simulation (dash-dot and circles), the QL simulation (dashed and dots) and the SSST IRFh (SSSTa), as well as the SSST for the equivalent spectrum to that obtained in NL as a consequence of modification of the IRFh spectrum by the nonlinear cascade (SSSTb). The bifurcation in the NL simulations occurs at  $\epsilon_c^{(NL)} \approx 4\epsilon_c$ . This figure shows that the structure of the jet in NL simulations is captured by the SSST if account is taken of the nonlinear modification of the spectrum. Parameters are  $\beta = 10$ ,  $r = 0.01$ ,  $r_m = 0.01$ .

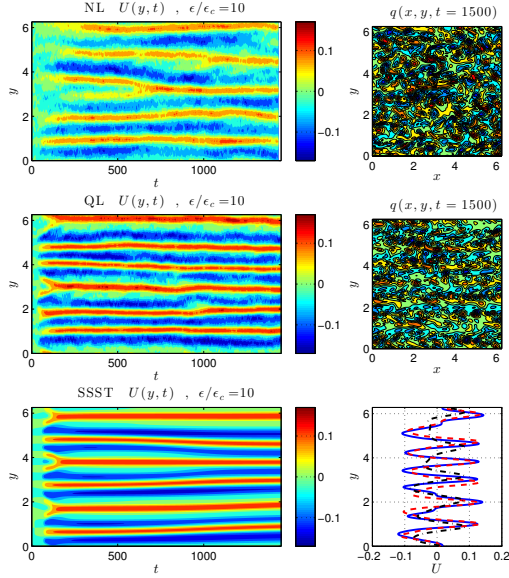


**Figure 14:** Hovmöller diagrams of jet emergence in NL, QL and SSST simulations with IRFh forcing at  $\epsilon = 10\epsilon_c$  and with  $K_f = 14$ ,  $\delta k_f = 1$ . Shown for the NL, QL and SSST simulations are  $U(y, t)$  (left panels) and for the NL and QL simulations the vorticity fields at  $t = 1500$  (top and middle right panels). Also shown are the equilibrium jets in the NL (dash-dot-black), QL (dashed - red), and SSST (solid - blue) simulation (bottom right panel). This figure shows that SSST predicts the structure, growth and equilibration of jets obtained in both the QL and NL simulations (cf. Fig. 4d). The jet maintained in the NL simulation has an amplitude which is 10% less than the amplitude of the jet of the QL simulation. Parameters are  $\beta = 10$ ,  $r = 0.01$ ,  $r_m = 0.01$ .

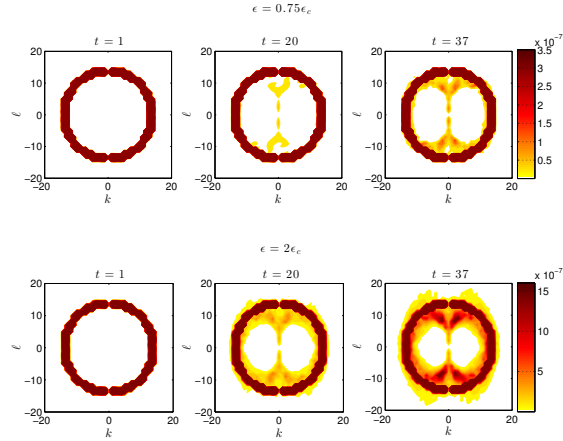


**Figure 15:** Evolution toward equilibrium of the energy spectrum,  $E_{k\ell} = \frac{1}{2} |\hat{q}_{k\ell}|^2 / (k^2 + \ell^2)$ , in NL under IRFh forcing with  $K_f = 14$  and  $\delta k_f = 1$ . At  $t = 0$  the spectrum is that of the homogeneous SSST equilibrium. Top panels: The spectrum at  $t = 1, 20, 37$  for  $\epsilon = 0.75\epsilon_c$ . Bottom panels: The spectrum at  $t = 1, 20, 37$  for  $\epsilon = 2\epsilon_c$ . The upscale energy cascade produces the familiar dumbbell spectrum. The distortion of the spectrum increases with  $\epsilon$ . The parameters are  $r = 0.01$ ,  $r_m = 0.01$  and  $\beta = 10$ .

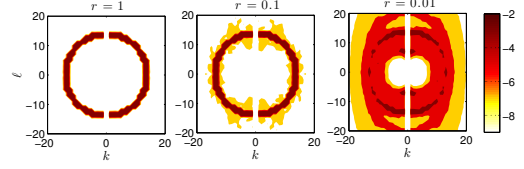


**Figure 16:** Equilibrium enstrophy spectrum,  $\log(2r|\hat{q}_{k\ell}|^2)$ , of NL simulations, in which perturbation-perturbation interactions are included but the  $k = 0$  component is excluded, for various damping rates,  $r$ . The example is for IRFh forcing at  $\epsilon = 2\epsilon_c$  and with  $K_f = 14$ ,  $\delta k_f = 1$ . Shown is the spectrum: (a) for linear damping coefficient  $r = 1$  (left panel), (b)  $r = 0.1$  (middle panel) and  $r = 0.01$  (right panel). The critical,  $\epsilon_c$ , is a function of  $r$  and is obtained from SSST. All spectra have been normalized by their maximum value. This figure shows that for relatively small damping the perturbation spectra in NL simulations are close to the SSST perturbation spectra while for weak damping the equilibrium spectrum in NL differs substantially from that in SSST. For the three cases  $\beta = 10$ .

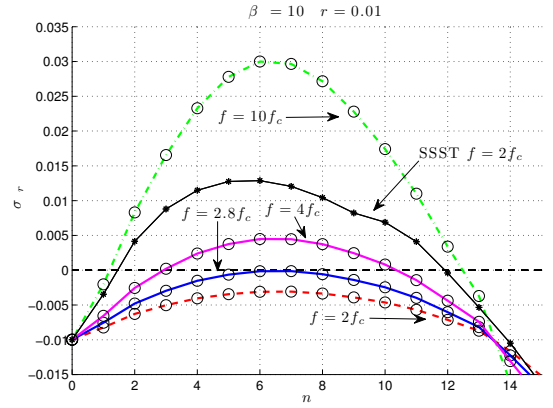


**Figure 17:** SSST jet instability growth rates for the equilibrium spectrum obtained in the NL dynamics subjected to IRFh forcing at  $K_f = 14$ ,  $\delta k_f = 1$  for  $r = 0.01$  (shown in the right panel of Fig. 16). Shown are the growth rates,  $\sigma_r$ , as a function of the meridional wavenumber,  $n$ , with forcing amplitude  $\epsilon = 2\epsilon_c$ ,  $\epsilon = 2.8\epsilon_c$ ,  $\epsilon = 4\epsilon_c$  and  $\epsilon = 10\epsilon_c$ . Also shown are the growth rates for the SSST equilibrium with IRFh forcing at  $\epsilon = 2\epsilon_c$  (solid-star line). This figure shows that the nonlinear interactions have modified the original ring spectrum making it more stable so that the modified flow state becomes unstable at  $\epsilon = 2.8\epsilon_c$  and  $n = 6$ . With this modification, the NL simulations agree with the predictions of the SSST analysis as shown in Fig. 13. Other parameters are  $\beta = 10$  and  $r_m = 0.01$ .

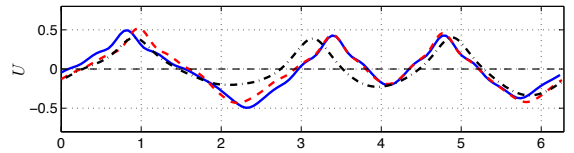


**Figure 18:** The mean jet structure,  $U(y)$ , for NL (dash-dot), QL (dashed) and SSST (solid) simulations for IRFh at  $K_f = 14$  with  $\delta k_f = 1$  for  $\epsilon = 100\epsilon_c$  and perturbation damping  $r = 0.01$ . There is good agreement between the jet structure in the NL simulation and the jets obtained with QL and SSST, despite the difference in the zmf index (cf. Fig. 13). The other parameters are  $\beta = 10$ ,  $r_m = 0.01$ .

obtained by NL dynamics will be different from the corresponding SSST equilibrium state due to this difference in the spectrum. The equilibrium spectrum obtained by taking a time average of long NL simulations, in which the  $k = 0$  component of the flow has been set to zero, is shown in Fig. 16 for various forcing amplitudes and damping rates. The departure of the NL spectra from the spectra of the QL and SSST equilibria is evident and this difference depends on the amplitude of the forcing and the linear damping coefficient,  $r$ . A necessary condition for obtaining agreement between NL and both SSST and QL dynamics is that the equilibrium spectrum of the SSST and QL dynamics be close to the equilibrium spectrum in the NL dynamics so that the stability analysis is performed on similar states.

The equilibrium spectrum obtained in the NL simulation does not differ appreciably from the spectrum of the forcing for IRFh at  $K_f = 14$  with  $\delta k_f = 1$  and linear damping  $r = 0.1$  (cf. Fig. 16). In such cases SSST successfully predicts the critical parameters for the emergence of jet structure in NL simulations as shown by the bifurcation diagram in Fig. 10 and, for the case of NIF, in Fig. 8.

SSST dynamics can be shown to accurately predict the emergence of zonal mean flows in the more weakly dissipated regime with  $r = 0.01$ , for which the NL spectra depart significantly from the spectra of the SSST homogeneous equilibrium, by performing the SSST stability analysis on the equilibrium spectrum obtained in the NL dynamics prior to emergence of the zonal mean jets. For example, with IRFh at  $K_f = 14$  and  $\delta k_f = 1$  and perturbation damping  $r = 0.01$ , formation of persistent finite amplitude zonal mean flows occurs in the NL simulations in the range  $3\epsilon_c < \epsilon < 4\epsilon_c$  instead of at  $\epsilon_c$  (cf. Fig. 13). We perform an SSST stability analysis with forcing covariance associated with the spectrum  $\epsilon \tilde{Q}_{k\ell} = 2r \langle |\tilde{q}_{k\ell}|^2 \rangle$ , where  $\langle |\tilde{q}_{k\ell}|^2 \rangle$  is the enstrophy spectrum obtained from the NL simulations in which the  $k = 0$  component was removed. We find that the equilibrium state with this spectrum is more stable than the original isotropic ring SSST equilibrium. This can be seen in Fig. 17 in which the growth rate of the SSST instability is shown as a function of the meridional wavenumber of the zonal mean perturbations for various forcing amplitudes. This calculation reveals that the NL-equivalent spectrum SSST equilibrium is marginally stable for  $\epsilon = 2.8\epsilon_c$ , and it produces SSST instability for  $\epsilon \geq 2.8\epsilon_c$ . This result agrees with the NL simulations which show emergence of persistent zonal mean flows for  $\epsilon \geq 2.8\epsilon_c$ . Moreover, SSST stability analysis on this NL-equivalent spectrum equilibrium state predicts that jet formation instability occurs at meridional wavenumber  $n = 5$  or  $n = 6$ , while the maximal instability for the isotropic ring spectrum that characterizes the corresponding SSST equilibrium occurs at the higher wavenumber  $n = 8$  (cf. Fig. 4d). In agreement with these predictions, zonal mean flows emerge in the NL simulations with  $n = 6$  while in both the QL and SSST simulation zonal mean flows

emerge with  $n = 9$ , as shown in Fig. 14. We find in addition, that the reduced amplitude of the zonal flows seen in the NL simulations (cf. Figs. 12 and 13) can be traced to the modification of the forcing spectrum by the nonlinear processes which reduces the forcing from the eddy field. The zmf that results in SSST using the NL modified spectrum is shown in Figs. 12 and 13 to agree with zmf obtained in the NL simulations<sup>1</sup>. This demonstrates that differences between the predictions of SSST stability theory and NL simulations for the emergence of zonal jets under weak damping results solely from the distortion of the equilibrium spectrum by the nonlinear interactions in the NL simulations.

SSST dynamics not only predicts the emergence of zonal jets but also predicts the finite amplitude equilibrium jets that result after the initial jet formation instability. These finite amplitude jets correspond to fixed points of the SSST dynamics. Here we compare the SSST predictions of finite amplitude jet structure with the results of NL and QL simulations. For the case of NIF (cf. Fig. 7), as well as for IRFh and IRFg, the jet equilibria obtained in QL and NL simulations are consistent with exact equilibria predicted by SSST. An example for IRFh strongly forced with  $\epsilon = 100\epsilon_c$  and with damping  $r = 0.01$  is shown in Fig. 18. This case demonstrates that a 20% difference in the zmf index between the NL, QL and SSST (cf. Fig. 13) is not reflected in a substantial disparity among the jets in NL, QL and SSST simulations.

## 9. Emergence of coherent non-zonal structures which strongly influence the spectrum of turbulence

In the NL integrations with IRFh forcing,  $r = r_m = 0.01$ , and energy input rates in the range  $\epsilon_c < \epsilon < \epsilon_c^{(NL)}$ , no persistent jets emerge, despite SSST supercriticality (cf. Fig. 19). Although no persistent zonal jets emerge in the NL simulation either, analysis of the NL perturbation field reveals the presence of coherent non-zonal structures that propagate westward at approximately the Rossby wave speed. The existence of similar structures in barotropic planetary turbulence has been reported in earlier studies (Sukoriansky et al. 2008). The presence of these non-zonal structures is evident in the concentration of power in the energy spectrum at  $(|k|, |\ell|) = (1, 7)$  and  $(|k|, |\ell|) = (1, 6)$  (cf. top panels of Fig. 20) and the coherence of these structures is clearly revealed in the Hovmöller diagrams shown in Fig. 21b-d. These structures are also present for energy input rates  $\epsilon > \epsilon_c^{(NL)}$ , for which jets have emerged in the NL simulation (Fig. 14). For example, the Hovmöller diagram for the

<sup>1</sup>The NL modified spectrum used to obtain the SSSTb bifurcation curve shown in Fig. 12 was obtained from the NL equilibrium spectrum at  $\epsilon = 4\epsilon_c$ . The spectrum used in Fig. 13 was obtained by similar means using an NL simulation at  $\epsilon = 2\epsilon_c$  (both with the  $k = 0$  component removed). The results are not sensitive to the choice of spectrum as long the broadening of the spectrum has been represented.

prominent non-zonal structures at this energy input rate is shown in Fig. 22 (the energy spectrum for this case is shown in the bottom panels of Fig. 20). Non-zonal coherent structures accompanying zonal jets have been reported in earlier studies and are referred to as satellite modes (Danilov and Gurarie 2002) or zonons (Sukoriansky et al. 2008).

SSST with the interpretation of the ensemble mean as a zonal mean does not allow energy to flow into these non-zonal structures, since only nonlinear interactions between the perturbations with the zonal components ( $k = 0$ ) are retained in this formulation. In order to be able to include non-zonal structures in the framework of SSST a different interpretation of the ensemble averages of SSST is required. Interactions between turbulence and non-zonal coherent structures can be supported within SSST if instead of interpreting the ensemble averaged fields in SSST as zonal averages we interpret them as slowly evolving variables obtained by Reynolds averaging of the fast scales. This interpretation was adopted in an SSST study of the formation of the dynamics of coherent structures in baroclinic turbulence (Bernstein 2009; Bernstein and Farrell 2010) and the implications of such a theory have been recently investigated in barotropic beta-plane turbulence (Bakas and Ioannou 2012, 2013b). Analysis of the SSST stability of the homogeneous equilibrium in barotropic beta-plane turbulence using this broader interpretation revealed that the structures that first become SSST unstable are often non-zonal, and only at higher energy input rates do the zonal structures become SSST unstable. Therefore, when the energy input rate reaches the value  $\epsilon_c$ , which is the SSST stability threshold for the emergence of zonal jets, the homogeneous background may be already SSST unstable to non-zonal structures. An example of the SSST growth rates of both zonal and non-zonal perturbations is shown in Fig. 23 for IRFh forcing with damping rates  $r = r_m = 0.01$  at the subcritical for the formation of jets energy input rate  $\epsilon = 0.75\epsilon_c$  and also at  $\epsilon = 2\epsilon_c$  (cf. Appendix D). In both cases the growth rates of non-zonal perturbations exceeds the growth rate of zonal perturbations and these non-zonal structures appear in NL simulations, as is evident in Fig. 20. The emergence of non-zonal structures modifies the background perturbation spectrum and the SSST instability of zonal flow perturbations is decreased (cf. Fig. 17). When this modified spectrum is used as the background spectrum, the SSST stability analysis predicts emergence of zonal flows in agreement with NL simulations (cf. the SSSTb bifurcation diagram in Figs. 12 and 13).

When the background spectrum is modified by the formation of these non-zonal structures, SSST stability analysis performed on the state characterized by the covariance of Eq. (29), which does not contain these structures, cannot predict accurately the emergence of jets in barotropic turbulence. Because this major modification of the spectrum occurs with the emergence of non-zonal structure, SSST stability accurately predicts the threshold for the emergence

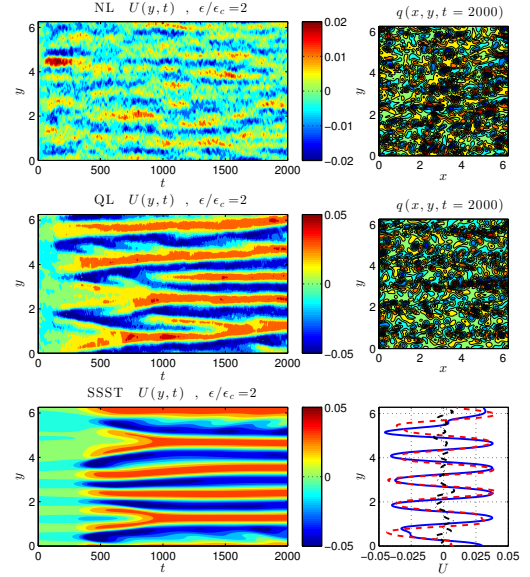


**Figure 19:** Hovmöller diagrams of jet emergence in NL, QL and SSST simulations with IRFh forcing at  $\epsilon = 2\epsilon_c$  and with  $K_f = 14$ ,  $\delta k_f = 1$ . Shown for the NL, QL and SSST simulations are  $U(y, t)$  (left panels) and for the NL and QL simulations the vorticity fields at  $t = 2000$  (top and middle right panels). Also shown are the equilibrium jets in the NL (dash-dot-black), QL (dashed - red), and SSST (solid - blue) simulation (bottom right panel). At  $\epsilon = 2\epsilon_c$  the NL simulation is subcritical but the  $n = 6$  structure of the least stable SSST mode is discernible (cf. Fig. 16). This figure shows that stable SSST eigenmodes can be excited by fluctuations in NL simulations in the subcritical regime. Parameters are  $\beta = 10$ ,  $r = 0.01$ ,  $r_m = 0.01$ .

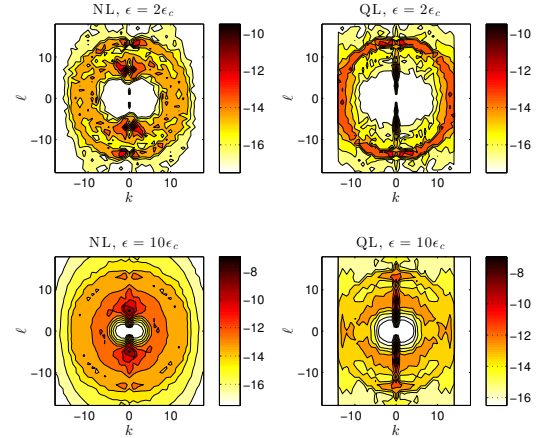


**Figure 20:** The statistical equilibrium energy spectrum,  $\log(E_{k\ell}) = \log(\frac{1}{2} |\hat{q}_{k\ell}|^2 / (k^2 + \ell^2))$ , for NL (left panels) and QL (right panels) integrations under IRFh forcing with  $K_f = 14$  and  $\delta k_f = 1$  at  $\epsilon = 2\epsilon_c$  (top panels) and  $\epsilon = 10\epsilon_c$  (bottom panels). While for  $\epsilon = 2\epsilon_c$  the NL integrations do not support zonal jets, we can see the accumulation of energy in the non-zonal mode  $(|k|, |\ell|) = (1, 7)$ . Also similar accumulation of energy in non-zonal structures is seen in the  $\epsilon = 10\epsilon_c$  for which persistent zonal jets form (cf. Fig. 14). These non-zonal structures are coherent and move westward (cf. Figs. 21 and 22). The QL integrations on the other hand do not support these non-zonal structures. Parameters:  $\beta = 10$ ,  $r = 0.01$ ,  $r_m = 0.01$ .



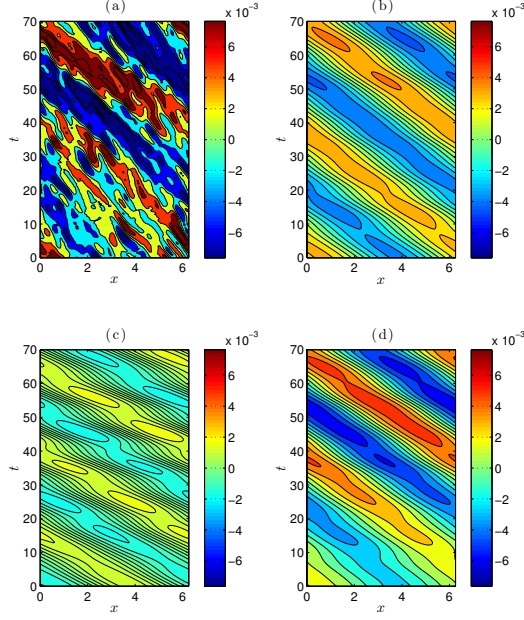


**Figure 21:** Hovmöller diagram of the non-zonal structures that are supported in the NL integration of Fig. 19. Panel (a): evolution of the streamfunction,  $\psi(x, y = y_0, t)$ , at latitude  $y_0 = \pi/4$ , obtained after the integration has reached statistical equilibrium. Using the time series of the streamfunction Fourier coefficients,  $\tilde{\psi}_{k\ell}$ , we construct the evolution of:  $\tilde{\psi}_{k,\ell}^{(y_0)}(x, t) = \tilde{\psi}_{k,\ell}(t) e^{i(kx + \ell y_0)} + \tilde{\psi}_{-k,-\ell}(t) e^{-i(kx + \ell y_0)}$ , for  $k, \ell > 0$ . Panel (b): evolution of  $\tilde{\psi}_{1,7}^{(y_0)}(x, t)$ . Panel (c): the evolution of  $\tilde{\psi}_{1,6}^{(y_0)}(x, t)$ . Panel (d): the sum of (b) and (c). We can see that almost all characteristics of the streamfunction  $\psi$  are captured by modes  $(|k|, |\ell|) = (1, 7)$  and  $(|k|, |\ell|) = (1, 6)$ . Parameters: IRFh forcing at  $K_f = 14$ ,  $\delta k_f = 1$  with  $\epsilon = 2\epsilon_c$ ,  $\beta = 10$ ,  $r = 0.01$ ,  $r_m = 0.01$ .

of zonal jets in NL simulations when this instability of non-zonal structures is suppressed or substantially reduced. Such a case occurs when the perturbation field is dissipated at rate  $r = 0.1$  while the mean flow is dissipated at the lower rate  $r_m = 0.01$ . SSST growth rates, shown in Fig. 24, show that with dissipations  $r = 0.1$  and  $r_m = r/10$  the non-zonal structures, which grow the most when  $r = r_m$ , have been stabilized and only the zonal perturbations are unstable. The agreement then between the NL, QL and SSST bifurcation diagrams shown in Figs. 8, 10 and 11 could then be attributed to the suppression or reduction of the instability of the non-zonal structures (for  $r = 0.01$  and  $r_m = r/10$  the non-zonal instability is severely inhibited but not suppressed altogether). This agreement of SSST predictions and NL dynamics for different damping coefficients is demonstrated for a wide range of damping parameters using NIF forcing in Fig. 25. For theoretical investigation, the jet formation instability can be studied in its simplest form by choosing a larger damping rate for the perturbations than for the zonal mean, so that the jets form before the complicating influence of the spectrum modification by the non-zonal structure instability, as we have done in some of the examples above.

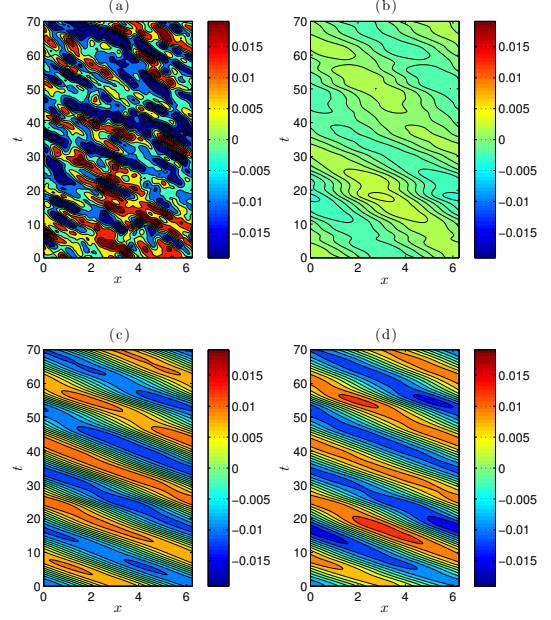


**Figure 22:** Hovmöller diagram of the non-zonal structures that are supported in the NL integration of Fig. 14. Panel (a): evolution of the perturbation streamfunction at a fixed latitude,  $\psi'(x, y = y_0, t)$ , at  $y_0 = 3.485$ , obtained after the integration has reached statistical equilibrium. The latitude  $y = 3.485$  lies between a westward and an eastward propagating jet. Panel (b): the evolution of  $\tilde{\psi}_{1,7}^{(y_0)}(x, t)$  (cf. caption of Fig. 21). Panel (c): evolution of  $\tilde{\psi}_{1,5}^{(y_0)}(x, t)$ . Panel (d): the sum of (b) and (c). We can see that almost all characteristics of the perturbation streamfunction  $\psi'$  are captured by mode  $(|k|, |\ell|) = (1, 5)$ . Parameters: IRFh forcing at  $K_f = 14$ ,  $\delta k_f = 1$  with  $\epsilon = 10\epsilon_c$ ,  $\beta = 10$ ,  $r = 0.01$ ,  $r_m = 0.01$ .

## 10. Association of stable SSST modes with stochastically excited intermittent jet structures in QL and NL

We can appreciate the control that the perturbation spectrum exerts on jet emergence by examining the case of forcing amplitude  $\epsilon = 2\epsilon_c$  with IRFh. At this forcing amplitude, SSST is structurally unstable and both SSST and QL simulations equilibrate to finite amplitude jets, as shown in Fig. 19. SSST stability analysis performed on the NL modified spectra (cf. Fig. 26) shows that at this forcing amplitude the asymptotic spectrum is subcritical to structural instability (cf. the SSST growth rates on the approximately asymptotic  $t = 250$  spectrum in Fig. 27). Consistent with this asymptotic stability, the NL simulation does not support coherent persistent jets (cf. Fig. 19). However, while in the NL simulation no coherent jets are seen, clear indications of jet structure can be seen, although these jets are intermittent in both space and time. In order to understand these observations we perform SSST stability analysis on the spectrum as it develops in the NL simulation. The developing spectrum, shown in Fig. 26, is obtained from a simulation initialized with a perturbation and mean flow



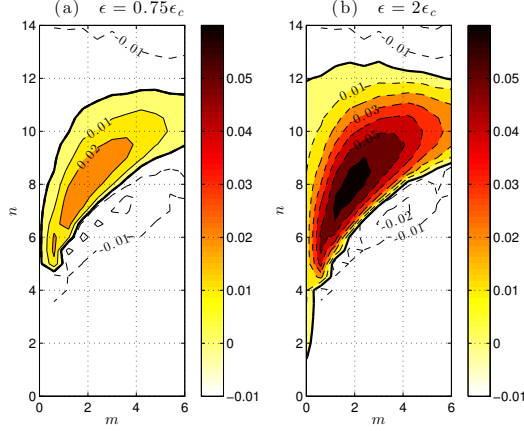


**Figure 23:** Growth rate,  $\sigma_r$ , of the SSST non-zonal eigenfunction,  $e^{i(mx+ny)}$ , as a function of zonal wavenumber  $m$  and meridional wavenumber,  $n$  for IRFh at  $\epsilon = 0.75\epsilon_c$  (panel (a)) and  $\epsilon = 2\epsilon_c$  (panel (b)). Here  $\epsilon_c$  is the critical energy input rate for the emergence of jets. The values at the axis,  $(0, n)$ , give the growth rate of the corresponding jet perturbation, as in Fig. 4. For  $\epsilon = 0.75\epsilon_c$  the  $m = 0$  jet eigenfunctions are stable but the non-zonal perturbations are unstable with maximum instability occurring at  $(m, n) = (2, 8)$ . For  $\epsilon = 2\epsilon_c$  the  $m = 0$  perturbations are unstable but the non-zonal perturbations are more strongly unstable, with maximum growth at  $(m, n) = (2, 8)$  and  $(m, n) = (1, 7)$ . An NL simulation at  $\epsilon = 2\epsilon_c$  accumulated energy at  $(|k|, |\ell|) = (1, 7)$  (cf. Fig. 20) while the vorticity field showed some accumulation at  $(|k|, |\ell|) = (2, 8)$  (cf. bottom right panel of Fig. 26). The stability boundary ( $\sigma_r = 0$ ) is marked with thick solid line and the unstable region is shaded. For both panels  $\beta = 10$  and  $r = r_m = 0.01$ .

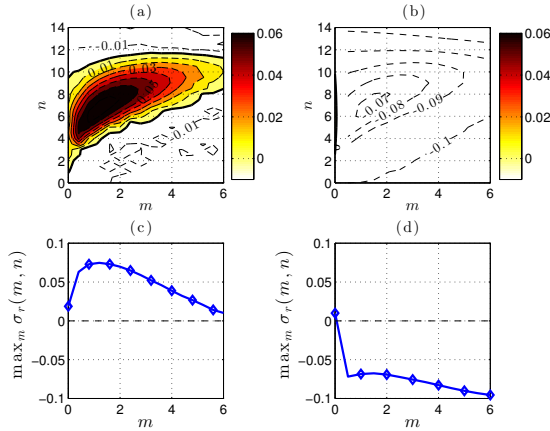


**Figure 24:** Panels (a)-(b): Growth rate,  $\sigma_r$ , of the SSST non-zonal eigenfunction,  $e^{i(mx+ny)}$ , as a function of zonal wavenumber  $m$  and meridional wavenumber,  $n$  for NIF with dissipation rate  $r = r_m = 0.01$  (panel (a)) and  $r = 0.1, r_m = r/10 = 0.01$  (panel (b)) and at energy input rate  $\epsilon = 2\epsilon_c$ . The stability boundary ( $\sigma_r = 0$ ) is marked with thick solid line and the unstable region is shaded. We can see that when  $r_m = r/10$  all non-zonal structures are stabilized. Panels (c)-(d): The maximum growth rate over all wavenumbers  $n$  as a function of the zonal wavenumber  $m$  for the two cases presented in panel (a) and (b) respectively. For both cases  $\beta = 10$ .

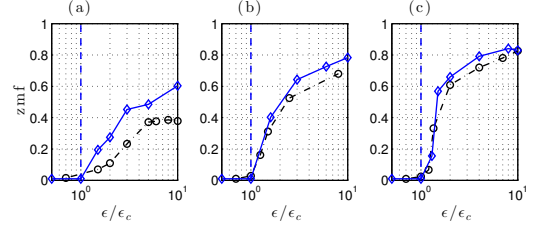


**Figure 25:** Bifurcation structure showing jet formation in SSST (solid) and NL (dash-dot) as a function of the energy input rate  $\epsilon/\epsilon_c$  for damping coefficients,  $r = 1, r_m = 0.1$  (panel (a)),  $r = 0.1, r_m = 0.01$  (panel (b)),  $r = 0.01, r_m = 0.001$  (panel (c)). The dashed line indicates the corresponding for each case critical energy input rate,  $\epsilon_c$  (for case (a):  $\epsilon_c = 4.17 \times 10^{-2}$ , for (b):  $\epsilon_c = 7.73 \times 10^{-5}$  and for (c):  $\epsilon_c = 2.75 \times 10^{-6}$ ). Other parameters  $\beta = 10$  and the forcing is NIF at  $k = 1, \dots, 14$ .

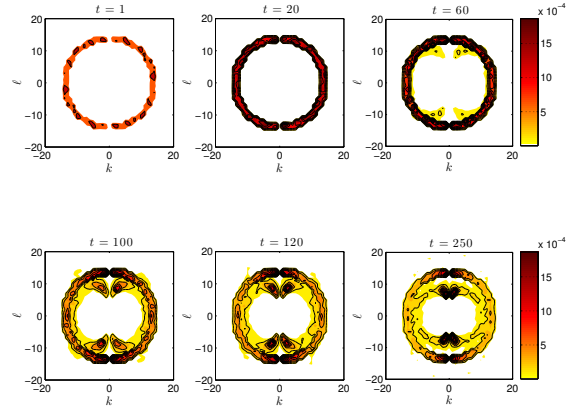


**Figure 26:** Evolution of the ensemble average enstrophy spectrum,  $|\bar{q}_{kl}|^2$ , for NL with isotropic ring forcing (IRFh) at wavenumber  $K_f = 14$ ,  $\delta k_f = 1$ , and forcing amplitude  $\epsilon = 2\epsilon_c$ . Parameters are  $\beta = 10$ ,  $r = 0.01$ ,  $r_m = 0.01$ .

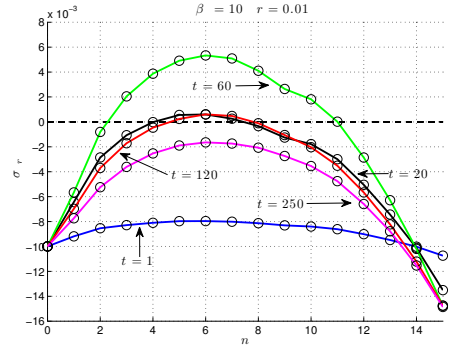


**Figure 27:** Instantaneous SSST growth rates,  $\sigma_r$ , as a function of jet meridional wavenumber,  $n$ , for equilibria with the evolving enstrophy spectra shown in Fig. 26. The evolving spectrum renders the NL simulation SSST unstable at  $t \approx 20$  and stabilizes it again at  $t \approx 120$ . Parameters are  $\beta = 10$ ,  $r = 0.01$ ,  $r_m = 0.01$ .

free state and the corresponding SSST growth rates associated with the developing spectrum are shown in Fig. 27. By  $t = 20$  the NL spectrum, having assumed the isotropic ring structure of the forcing, becomes SSST unstable. This structural instability is evident in the incipient formation of jet structure in the NL simulation at  $t = 50$  in Fig. 19. As the spectrum further evolves, the SSST growth rates fall and the spectrum supports only stable modes for  $t > 120$ , with decay rates asymptotically approaching those corresponding to  $t = 250$  in Fig. 27. For these asymptotic perturbation spectra, SSST stability analysis reveals a manifold of decaying modes among which the least damped modes are jets with meridional wavenumber  $n = 5, 6, 7, 8$ . There is clear evidence of zonal structure in the NL simulations in the form of a superposition of the  $n = 5, 6, 7, 8$  least damped modes of the SSST stability analysis (cf. Fig. 17). These damped modes are excited by the fluctuations associated with realizations of the stochastic forcing in NL simulations. Similar excitation of intermittent jets associated with these damped modes arise in QL simulations with SSST subcritical stochastic forcing. An example simulation (cf. Fig. 28) shows these intermittent jets both in QL and NL simulations under SSST subcritical forcing. Confirmation that these intermittent jets result from fluctuation excitation of the SSST damped modes is given in the bottom panel of Fig. 28, where the intermittent jets resulting from stochastic forcing of the SSST modes themselves are shown. This diagram was obtained by plotting

$$U(y, t) = \text{Re} \left[ \sum_{n=1}^N \alpha_n(t) e^{iny} \right], \quad (33)$$

with  $\alpha_n$  independent red noise processes, associated with the damping rates,  $-\sigma(n)$ , of the first  $N = 15$  SSST least damped modes. These  $\alpha_n$  are obtained from the Langevin equation,

$$\frac{d\alpha_n}{dt} = \sigma(n) \alpha_n + \xi(t), \quad (34)$$

with  $\xi(t)$  a  $\delta$ -correlated complex valued random variable.

The fluctuation-free SSST simulations reveal persistent jet structure by the inception of the SSST instability which occurs only at supercritical forcing. However, in the QL and NL simulations fluctuations excite the damped manifold of modes predicted by the SSST analysis to exist at subcritical forcing amplitudes. This observation confirms the reality of the wave/mean flow interaction manifold of stable modes. This emergence of structure at subcritical forcing provides an explanation for the observation of the so-called latent zonal jets in the oceans (Berloff et al. 2009, 2011; Cravatte et al. 2012).

In NL and QL simulations these stable modes predicted by SSST are increasingly excited as the critical bifurcation point in parameter space is approached, because their damping rate vanishes at the bifurcation. The associated increase in

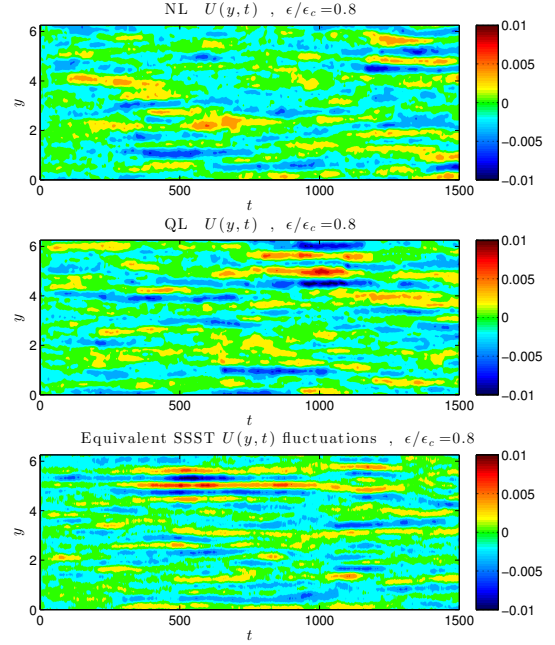


**Figure 28:** Hovmöller diagrams of intermittent jet structure in NL and QL simulations at subcritical forcing  $\epsilon = 0.8\epsilon_c$ . Shown are  $U(y, t)$  resulting for: NL (top) and QL (middle) simulations and the  $U(y, t)$  that results from random excitation of the SSST damped modes (bottom panel). These plots were obtained using IRFh forcing with  $K_f = 14$ ,  $\delta k_f = 1$  and  $r = 0.1$  (cf. Fig. 10). This figure shows that the manifold of SSST damped modes are revealed by being excited in the fluctuating NL and QL simulations. Other parameters are  $\beta = 10$ ,  $r_m = 0.01$ .

zonal mean flow energy on approach to the bifurcation in NL and QL simulations, obscures the exact location of the bifurcation point in NL and QL simulations compared to the fluctuation-free SSST simulations for which the bifurcation is exactly coincident with the inception of instability (i.e. Figs. 8, 10 and 11).

## 11. Realizability of multiple equilibria found by SSST in NL simulations

As is commonly found in nonlinear systems, the finite amplitude equilibria predicted by SSST are not necessarily unique and multiple equilibria can occur for the same parameters. SSST provides a theoretical framework within which to explore these multiple equilibria and determine their attractor basins in the parameter space. For supercritical parameter values the SSST instabilities with different zonal flow wavenumber (cf. Fig. 4) may give rise to multiple jet equilibria. An example of two such SSST equilibria are shown in Fig. 29 together with their associated NL simulations. As the parameters change these equilibria may cease to exist or become SSST unstable. This change in the attractor structure manifests as the jet merger phenomenon

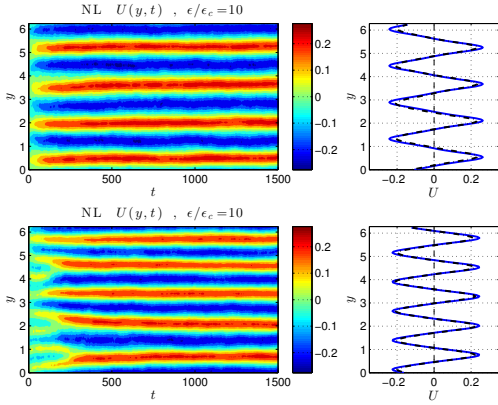


**Figure 29:** Realizations in NL simulations of multiple equilibria predicted by SSST. Left panels: Hovmöller diagrams of NL simulations showing the equilibrium with 4 jets (top) and with 5 jets (bottom). Right panels: comparison of the SSST equilibrium jets (solid) with the average jets obtained from the NL simulation (dashed). Parameters: NIF forcing at  $k = 1, \dots, 14$  with energy input rate  $\epsilon = 10\epsilon_c$ ,  $\beta = 10$ ,  $r = 0.1$ ,  $r_m = 0.01$ .

seen in most of the Hovmöller diagrams of jet evolution. Similar multiple equilibria have been found in SSST studies of barotropic turbulence on a beta-plane with the mean flow being relaxed to a background flow (Farrell and Ioannou 2003) and in SSST studies of baroclinic turbulence (Farrell and Ioannou 2008, 2009) and the hypothesis has been advanced that the existence of such multiple jet equilibria underlie the abrupt climate transitions found in the record of Earth’s climate (Farrell and Ioannou 2003; Wunsch 2003).

## 12. Conclusions

In this work the predictions of SSST for jet formation in barotropic beta-plane turbulence were compared with results obtained using QL and NL simulations. The bifurcation structure predicted by SSST for the emergence of zonal jets from a homogeneous turbulent state was confirmed by both the QL and NL simulations. Moreover, the finite amplitude equilibrium jets found in NL and QL simulations were found to be as predicted by the fixed point solutions of SSST. The spectrum of turbulence was found to be substantially modified by the emergence of non-zonal coherent structures. When account is taken of the modification of the turbulent spectrum resulting from these coherent structures SSST provides quantitative agreement with the threshold values for the emergence of jets in NL.

These results confirm that jet emergence in barotropic beta-plane turbulence results from the cooperative mean flow/perturbation instability that is captured by SSST. Moreover, the physical reality of the manifold of modes arising from cooperative interaction between incoherent turbulence and coherent jets, which is revealed by SSST, was verified in this work by relating the excitation of the spectrum of

damped SSST modes to observations of latent jets in both QL and NL simulations.

SSST provides an autonomous, deterministic nonlinear closure of the turbulent dynamics at second order that provides a vehicle for further analytic investigation of the dynamics of coherent structures in turbulent flows.

## Acknowledgments.

The authors would like to acknowledge discussions with N. Bakas, F. Bouchet, K. Srinivasan and W. Young. Navid Constantinou acknowledges the support of the Alexander S. Onassis Public Benefit Foundation. Brian Farrell was supported by NSF AGS-1246929 and ATM-0736022. Brian Farrell and Petros Ioannou acknowledge the hospitality during June 2012 of the Aspen Center for Physics (supported by NSF under grant No. 1066293) where part of this paper was written. Petros Ioannou acknowledges the generous support of the John S. Latsis Foundation under “Research Projects 2011”.

## APPENDIX A

### Numerical details and parameters

Periodicity in the square channel  $[0, 2\pi] \times [0, 2\pi]$  implies that the permissible zonal and meridional wavenumbers,  $(k, \ell)$ , are integers and the NIF and IRFh or IRFg forcing is limited to these integer wavenumbers. The coefficient of linear damping for the mean flow in all simulations is  $r_m = 0.01$ . The perturbations are damped at the rate  $r = 0.1$  or at the rate  $r = 0.01$ . In all simulations  $\beta = 10$ .

Both the nonlinear simulation (NL) of Eq. (1) and the quasi-linear simulations (QL) of Eqs. (4) are done with a pseudospectral Fourier code. The maximum resolved wavenumbers are  $k_{\max} = N_x/2$  and  $\ell_{\max} = N_y/2$  and the maximum resolved total wavenumber  $K_{\max} = (k_{\max}^2 + \ell_{\max}^2)^{1/2}$ . For the time integration we use a fourth order Runge-Kutta method (RK4) using a Godunov step for integrating the stochastic forcing.

In all calculations hyperviscosity was added with coefficient of  $\nu_4$  for numerical stability. The coefficient was chosen as

$$\nu_4 = \frac{0.5}{K_{\max}^4 \delta t}, \quad (\text{A1})$$

where  $\delta t$  is the time step. In all our calculations  $\delta t = 2.5 \times 10^{-3}$  and  $N_x = N_y = 256$ , which imply  $\nu_4 = 1.86 \times 10^{-7}$ .

The stochastic forcing at the  $j$ -th time step is obtained from:

$$\xi_{km}(t_j) = \frac{\eta_j + i\theta_j}{\sqrt{2\delta t}}, \quad (\text{A2})$$

where  $\eta_j$  and  $\theta_j$ ,  $j = 1, 2, \dots$  are independent, normally distributed, random variables with zero mean and unit standard deviation. The phase of  $\xi_{km}$  is uniformly distributed in

$[0, 2\pi]$ . The  $\sqrt{\delta t}$  in the denominator ensures that the forcing maintains constant variance as temporal resolution changes and the  $\sqrt{2}$  ensures that  $\xi_{km}$  has unit variance, i.e. that in the limit  $\delta t \rightarrow 0$ :  $\int_{-\infty}^{\infty} \langle \xi_{km}(t) \xi_{km}^*(t') \rangle dt' = 1$ .

## APPENDIX B

### Calculation of the energy input rate

The domain averaged energy input rate by the stochastic forcing,  $F$ , is:

$$\varepsilon = - \int \frac{dx}{L_x} \frac{dy}{L_y} \psi' F. \quad (\text{B1})$$

We Fourier expand all fields as in (5). When  $y$  is discretized, the Fourier coefficient of the streamfunction for zonal wavenumber  $k$ ,  $\hat{\psi}_k(y, t)$ , is related to vorticity,  $\hat{q}_k(y, t)$ , by  $\hat{\psi}_k(t) = \mathbf{\Delta}_k^{-1} \hat{\mathbf{q}}_k(t)$  where  $\hat{\psi}_k$  and  $\hat{\mathbf{q}}_k$  are column vectors and  $\mathbf{\Delta}_k^{-1}$  the inverse of the matrix representation of  $\partial_{yy} - k^2$ . If the evolution of  $\hat{\mathbf{q}}_k$  is governed by Eq. (15) (with  $\epsilon = 1$ ) then it has solution (in matrix form):

$$\hat{\mathbf{q}}_k(t) = \exp(\mathbf{A}_k t) \hat{\mathbf{q}}_k(0) + \int_0^t \exp[\mathbf{A}_k(t-s)] \mathbf{F}_k \boldsymbol{\xi}_k(s) ds, \quad (\text{B2})$$

where  $\boldsymbol{\xi}_k$  is the column vector with elements  $[\boldsymbol{\xi}_k]_\ell = \xi_{k\ell}$ . Assuming ergodicity, the zonal average in Eq. (B1) can be replaced by an ensemble average and then converted in matrix form, obtaining:

$$\begin{aligned} \varepsilon &= - \int \frac{dy}{L_y} \langle \psi' F \rangle \\ &= - \int \frac{dy}{L_y} \frac{1}{4} \left\langle \sum_{k=1}^{N_k} \left( \hat{\psi}_k \hat{F}_k^* + \hat{\psi}_k^* \hat{F}_k \right) \right\rangle \\ &= - \frac{1}{4N_y} \left\langle \sum_{k=1}^{N_k} \text{Tr} \left[ \hat{\psi}_k \left( \mathbf{F}_k \boldsymbol{\xi}_k \right)^\dagger + \left( \mathbf{F}_k \boldsymbol{\xi}_k \right) \hat{\psi}_k^\dagger \right] \right\rangle, \quad (\text{B3}) \end{aligned}$$

with  $\text{Tr}$  denoting the trace of a matrix. Because the noise processes are independent and temporally delta correlated, satisfying  $\langle \xi_{km}(t) \xi_{k'm'}^*(t') \rangle = \delta_{kk'} \delta_{mm'} \delta(t - t')$ , we obtain, using (B2), that both terms of the sum in (B3) are independent of the state of the system and equal to

$$- \frac{1}{2} \text{Tr} \left( \mathbf{\Delta}_k^{-1} \mathbf{F}_k \mathbf{F}_k^\dagger \right). \quad (\text{B4})$$

Consequently, energy is injected at the rate:

$$\varepsilon = \sum_{k=1}^{N_k} \varepsilon_k = \sum_{k=1}^{N_k} - \frac{1}{4N_y} \text{Tr} \left( \mathbf{\Delta}_k^{-1} \mathbf{Q}_k \right). \quad (\text{B5})$$

This expression can be rewritten in terms of the Fourier coefficients of the forcing covariance,  $\hat{Q}_{k\ell}$  (cf. Eq. (11)). The

matrix covariance  $\mathbf{Q}_k$  is related to coefficients  $\hat{Q}_{k\ell}$  through Eq. (19). The matrix  $\mathbf{\Delta}_k^{-1} \mathbf{Q}_k$  has elements:

$$\begin{aligned} \left[ \mathbf{\Delta}_k^{-1} \mathbf{Q}_k \right]_{mn} &= \sum_{r=1}^{N_y} \left[ \mathbf{\Delta}_k^{-1} \right]_{mr} \left[ \mathbf{Q}_k \right]_{rn} \\ &= \sum_{\ell=-N_y/2}^{N_y/2-1} \sum_{r=1}^{N_y} \hat{Q}_{k\ell} \left[ \mathbf{\Delta}_k^{-1} \right]_{mr} e^{i\ell(y_r - y_n)} \\ &= - \sum_{\ell=-N_y/2}^{N_y/2-1} \hat{Q}_{k\ell} \frac{e^{i\ell(y_m - y_n)}}{k^2 + \ell^2}. \quad (\text{B6}) \end{aligned}$$

In the second equality the first summation is over meridional wavenumbers and the second over discretization points. Therefore the energy input rate is:

$$\varepsilon = \frac{1}{2} \sum_{k=1}^{N_k} \sum_{\ell=-N_y/2}^{N_y/2-1} \frac{\hat{Q}_{k\ell}}{2(k^2 + \ell^2)}. \quad (\text{B7})$$

(The forcing covariance  $Q$  is symmetric to interchange of points  $(x_a, y_a)$  and  $(x_b, y_b)$ . This implies that coefficients  $\hat{Q}_{k\ell}$  are real.)

We have normalized all forcing structures introduced in section 5 so that their energy input rate is unity, and thus the total energy input rate in the NL, QL and SSST simulations is equal to  $\epsilon$ .

## APPENDIX C

### Determining the SSST stability of the homogeneous state

Equations (30) determine the SSST stability of the equilibrium state. Because of the presence of the imaginary part in Eq. (30a), in order to proceed with eigenanalysis of this system we need to treat the real and imaginary part of the perturbation covariances as independent variables. Writing the perturbation covariances as  $\delta \mathbf{C}_k = \delta \mathbf{C}_{k,R} + i \delta \mathbf{C}_{k,I}$ , and the perturbation operators as  $\delta \mathbf{A}_k = -ik [\delta \mathbf{U} - (\delta \mathbf{U})_{yy} \mathbf{\Delta}_k^{-1}] = i \delta \mathbf{A}_{k,I}$  and separating the real and imaginary part the equilibrium operators and covariances:  $\mathbf{A}_k^E = \mathbf{A}_{k,R}^E + i \mathbf{A}_{k,I}^E$  and  $\mathbf{C}_k^E = \mathbf{C}_{k,R}^E + i \mathbf{C}_{k,I}^E$ , we obtain the equivalent to (30) real coefficient system:

$$\partial_t \delta \mathbf{U} = \sum_{k=1}^{N_k} \frac{1}{2} \text{vecd} \left( -k \mathbf{\Delta}_k^{-1} \delta \mathbf{C}_{k,I} \right) - r_m \delta \mathbf{U}, \quad (\text{C1a})$$



$$\partial_t \delta \mathbf{C}_R = \mathbf{A}_R^E \delta \mathbf{C}_R + \delta \mathbf{C}_R \left( \mathbf{A}_R^E \right)^T - \mathbf{A}_I^E \delta \mathbf{C}_I + \delta \mathbf{C}_I \left( \mathbf{A}_I^E \right)^T - \delta \mathbf{A}_I \mathbf{C}_I^E + \mathbf{C}_I^E \delta \mathbf{A}_I^T, \quad (\text{C1b})$$

$$\partial_t \delta \mathbf{C}_I = \mathbf{A}_I^E \delta \mathbf{C}_I - \delta \mathbf{C}_R \left( \mathbf{A}_R^E \right)^T + \mathbf{A}_R^E \delta \mathbf{C}_I + \delta \mathbf{C}_I \left( \mathbf{A}_R^E \right)^T + \delta \mathbf{A}_I \mathbf{C}_R^E - \mathbf{C}_R^E \delta \mathbf{A}_I^T, \quad (\text{C1c})$$

in which the subscript  $k$  in all the variables in Eqs. (C1b) and (C1c) has been omitted. The asymptotic stability of (C1) is determined by assuming solutions of the form

$$(\delta \hat{\mathbf{U}}, \delta \hat{\mathbf{C}}_{k,R}, \delta \hat{\mathbf{C}}_{k,I}) e^{\sigma t} \quad \text{for } k = 1, \dots, N_k, \quad (\text{C2})$$

with  $\delta \mathbf{A}_{k,I} = \delta \hat{\mathbf{A}}_{k,I} e^{\sigma t}$  and by determining the eigenvalues,  $\sigma$ , and the eigenfunctions of the system:

$$\sigma \delta \hat{\mathbf{U}} = \sum_{k=1}^{N_k} \frac{1}{2} \text{vecd} \left( -k \mathbf{\Delta}_k^{-1} \delta \hat{\mathbf{C}}_{k,I} \right) - r_m \delta \hat{\mathbf{U}}, \quad (\text{C3a})$$

$$\sigma \delta \hat{\mathbf{C}}_R = \mathbf{A}_R^E \delta \hat{\mathbf{C}}_R + \delta \hat{\mathbf{C}}_R \left( \mathbf{A}_R^E \right)^T - \mathbf{A}_I^E \delta \hat{\mathbf{C}}_I + \delta \hat{\mathbf{C}}_I \left( \mathbf{A}_I^E \right)^T - \delta \hat{\mathbf{A}}_I \mathbf{C}_I^E + \mathbf{C}_I^E \delta \hat{\mathbf{A}}_I^T, \quad (\text{C3b})$$

$$\sigma \delta \hat{\mathbf{C}}_I = \mathbf{A}_I^E \delta \hat{\mathbf{C}}_I - \delta \hat{\mathbf{C}}_R \left( \mathbf{A}_R^E \right)^T + \mathbf{A}_R^E \delta \hat{\mathbf{C}}_I + \delta \hat{\mathbf{C}}_I \left( \mathbf{A}_R^E \right)^T + \delta \hat{\mathbf{A}}_I \mathbf{C}_R^E - \mathbf{C}_R^E \delta \hat{\mathbf{A}}_I^T. \quad (\text{C3c})$$

In most cases direct eigenanalysis of this system is computationally prohibitive because it involves eigenanalysis of matrices of dimension  $(2N_k N^2 + N) \times (2N_k N^2 + N)$  if  $N$  grid points are used to approximate the functions and  $N_k$  zonal wavenumbers are forced. In this section we describe an iterative method that can produce solutions to this stability problem for large  $N$ . The method is a generalization of the adiabatic approximation used in earlier studies (Farrell and Ioannou 2003, 2007; Bakas and Ioannou 2011).

When (C3) has eigenvalues with  $\text{Re}(\sigma) > 0$  the equilibrium is SSST unstable. When  $\sigma$  is complex the eigenfunctions  $\delta \hat{\mathbf{U}}$ ,  $\delta \hat{\mathbf{C}}_{k,R}$ ,  $\delta \hat{\mathbf{C}}_{k,I}$  and  $\delta \hat{\mathbf{A}}_{k,I}$  will be complex. Realizable solutions can then be formed by superposing to these eigenfunctions their complex conjugates, which are also eigenfunctions. Note that the perturbation covariances are required to be only Hermitian and need not be positive definite (for a discussion of eigenvalue problems involving covariances cf. Farrell and Ioannou (2002)).

Because of the periodic boundary conditions the mean flow eigenfunctions  $\delta \hat{\mathbf{U}}$  are a superposition of harmonics. However, because the equilibrium state has zero mean flow it can be shown that the eigenfunctions  $\delta \hat{\mathbf{U}}$  are single harmonics,

$$\delta \hat{\mathbf{U}}_n = e^{iny}, \quad (\text{C4})$$

and Eq. (C3a) becomes:

$$\sigma e^{iny} = \sum_{k=1}^{N_k} \frac{1}{2} \text{vecd} \left( -k \mathbf{\Delta}_k^{-1} \delta \hat{\mathbf{C}}_{k,I} \right) - r_m e^{iny}. \quad (\text{C5})$$

The number of jets that will emerge in the channel, if the equilibrium is unstable, is  $n$ . Equation (C5) can be regarded as an equation for  $\sigma$  given that  $\delta \hat{\mathbf{C}}_{k,I}$  satisfies the coupled equations Eqs. (C3b) and (C3c) and is therefore a function of  $\sigma$  and  $n$ . Having transformed Eq. (C5) into an equation for  $\sigma$  for a given  $n$  we can determine the eigenvalues by an iteration.

It is advantageous to solve Eqs. (C3b) and (C3c) for the variables

$$\delta \hat{\mathbf{T}}_{k,P} = \delta \hat{\mathbf{C}}_{k,R} + i \delta \hat{\mathbf{C}}_{k,I}, \quad \delta \hat{\mathbf{T}}_{k,M} = \delta \hat{\mathbf{C}}_{k,R} - i \delta \hat{\mathbf{C}}_{k,I}, \quad (\text{C6})$$

which satisfy the decoupled Sylvester equations:

$$0 = (\mathbf{A}^E - \sigma \mathbf{I}) \delta \hat{\mathbf{T}}_{k,P} + \delta \hat{\mathbf{T}}_{k,P} \left( \mathbf{A}^E \right)^\dagger + \left( i \delta \hat{\mathbf{A}}_{n,I} \right) \mathbf{C}^E + \mathbf{C}^E \left( -i \delta \hat{\mathbf{A}}_{n,I}^T \right), \quad (\text{C7a})$$

$$0 = \left[ (\mathbf{A}^E)^* - \sigma \mathbf{I} \right] \delta \hat{\mathbf{T}}_{k,M} + \delta \hat{\mathbf{T}}_{k,M} \left[ (\mathbf{A}^E)^* \right]^\dagger + \left( -i \delta \hat{\mathbf{A}}_{n,I} \right) \left( \mathbf{C}^E \right)^* + \left( \mathbf{C}^E \right)^* \left( i \delta \hat{\mathbf{A}}_{n,I}^T \right). \quad (\text{C7b})$$

(N.B. If the eigenvectors  $\delta \hat{\mathbf{C}}_{k,R}$  and  $\delta \hat{\mathbf{C}}_{k,I}$  are complex, despite the notation, then  $\text{Re}(\delta \hat{\mathbf{T}}_{k,P}) \neq \delta \hat{\mathbf{C}}_{k,R}$  and  $\text{Im}(\delta \hat{\mathbf{T}}_{k,P}) \neq \delta \hat{\mathbf{C}}_{k,I}$ .)

Hyperviscosity can be easily included in the calculation of the SSST stability of the homogeneous equilibrium. We only need to include the hyperviscosity term in the  $\mathbf{A}^E$  operator and equilibrium covariance,  $\mathbf{C}^E$ .

## APPENDIX D

### Determining the SSST stability of the homogeneous state to non-zonal perturbation

The SSST stability of a homogeneous background state to non-zonal perturbations of the form  $e^{\sigma t} e^{i(mx+ny)}$ , in which  $m$  is the zonal wavenumber of the perturbations and  $n$  is the meridional wavenumber of perturbations, is determined by the eigenvalues  $\sigma$  that solve for each  $(m, n)$  the equation:

$$\begin{aligned} & \left[ \sigma + r_m \delta_{m0} + r(1 - \delta_{m0}) \right] N^2 - im\beta = \\ & = \sum_k \sum_\ell 2(nk - m\ell) \left[ mn(k_+^2 - \ell_+^2) - (m^2 - n^2)k_+\ell_+ \right] \times \\ & \quad \times (K^2 - N^2) \frac{\epsilon \tilde{Q}_{k\ell}}{2r} \Bigg/ \left[ (\sigma + 2r)K^4 K_s^2 + \right. \\ & \quad \left. + 2i\beta k_+(k_+m + \ell_+n)K^2 - im\beta K^2(K^2 + K_s^2)/2 \right]. \end{aligned} \quad (\text{D1})$$

In the above equation,  $N^2 = m^2 + n^2$ ,  $K^2 = k^2 + \ell^2$ ,  $K_s^2 = (k+m)^2 + (\ell+n)^2$ ,  $k_+ = k + m/2$ ,  $\ell_+ = \ell + n/2$  and  $\delta_{ij}$  is



Kronecker's delta and  $\tilde{Q}_{k\ell}$  are the Fourier coefficients of the forcing covariance as defined in Eq. (13). This form of the equation is appropriate for a square channel of length  $2\pi$  and the summations are over the integer wavenumbers  $k$  and  $\ell$ . The derivation of the above equation is found in Bakas and Ioannou (2013b). For a specified forcing with spectrum  $\tilde{Q}_{k\ell}$  the growth rates are obtained using Newton's method.

## REFERENCES

- Bakas, N. A. and P. J. Ioannou, 2011: Structural stability theory of two-dimensional fluid flow under stochastic forcing. *J. Fluid Mech.*, **682**, 332–361, doi:[10.1017/jfm.2011.228](https://doi.org/10.1017/jfm.2011.228).
- Bakas, N. A. and P. J. Ioannou, 2012: Emergence of large scale structure in planetary turbulence. *Phys. Rev. Lett.*, (sub judice, [arXiv: 1211.6582](https://arxiv.org/abs/1211.6582)).
- Bakas, N. A. and P. J. Ioannou, 2013a: On the mechanism underlying the spontaneous emergence of barotropic zonal jets. *J. Atmos. Sci.*, doi:[10.1175/JAS-D-12-0102.1](https://doi.org/10.1175/JAS-D-12-0102.1), in press.
- Bakas, N. A. and P. J. Ioannou, 2013b: A theory for the emergence of coherent structures in beta-plane turbulence. *J. Fluid Mech.*, (sub judice).
- Baldwin, M. P., P. B. Rhines, H.-P. Huang, and M. E. McIntyre, 2007: The jet-stream conundrum. *Science*, **39**, 467–468, doi:[10.1126/science.1131375](https://doi.org/10.1126/science.1131375).
- Berloff, P., I. Kamenkovich, and J. Pedlosky, 2009: A model of multiple zonal jets in the oceans: Dynamical and kinematical analysis. *J. Phys. Oceanogr.*, **39**, 2711–2734, doi:[10.1175/2009JPO4093.1](https://doi.org/10.1175/2009JPO4093.1).
- Berloff, P., S. Karabasov, J. Farrar, and I. Kamenkovich, 2011: On latency of multiple zonal jets in the oceans. *J. Fluid Mech.*, **686**, 534–567, doi:[10.1017/jfm.2011.345](https://doi.org/10.1017/jfm.2011.345).
- Bernstein, J., 2009: Dynamics of turbulent jets in the atmosphere and ocean. Ph.D. thesis, Harvard University.
- Bernstein, J. and B. F. Farrell, 2010: Low frequency variability in a turbulent baroclinic jet: Eddy-mean flow interactions in a two-level model. *J. Atmos. Sci.*, **67** (2), 452–467, doi:[10.1175/2009JAS3170.1](https://doi.org/10.1175/2009JAS3170.1).
- Bouchet, F. and A. Venaille, 2012: Statistical mechanics of two-dimensional and geophysical flows. *Phys. Rep.*, **515** (5), 227–295, doi:[10.1016/j.physrep.2012.02.001](https://doi.org/10.1016/j.physrep.2012.02.001).
- Charney, J. G. and J. G. DeVore, 1979: Multiple flow equilibria in the atmosphere and blocking. *J. Atmos. Sci.*, **36**, 1205–1216, doi:[10.1175/1520-0469\(1979\)036<1205:MFEITA>2.0.CO;2](https://doi.org/10.1175/1520-0469(1979)036<1205:MFEITA>2.0.CO;2).
- Connaughton, C. P., B. T. Nadiga, S. V. Nazarenko, and B. E. Quinn, 2010: Modulational instability of Rossby and drift waves and generation of zonal jets. *J. Fluid Mech.*, **645**, 207–231, doi:[10.1017/S0022112010000510](https://doi.org/10.1017/S0022112010000510).
- Cravatte, S., W. S. Kessler, and F. Marin, 2012: Intermediate zonal jets in the tropical pacific ocean observed by Argo floats. *J. Phys. Oceanogr.*, **42** (9), 1475–1485, doi:[10.1175/JPO-D-11-0206.1](https://doi.org/10.1175/JPO-D-11-0206.1).
- Danilov, S. and D. Gurarie, 2002: Rhines scale and spectra of the  $\beta$ -plane turbulence with bottom drag. *Phys. Rev. E*, **65** (6), 67 301, doi:[10.1103/PhysRevE.65.067301](https://doi.org/10.1103/PhysRevE.65.067301).
- DelSole, T., 2001: A simple model for transient eddy momentum fluxes in the upper troposphere. *J. Atmos. Sci.*, **58**, 3019–3035, doi:[10.1175/1520-0469\(2001\)058<3019:ASMFTE>2.0.CO;2](https://doi.org/10.1175/1520-0469(2001)058<3019:ASMFTE>2.0.CO;2).
- DelSole, T. and B. F. Farrell, 1996: The quasi-linear equilibration of a thermally maintained stochastically excited jet in a quasigeostrophic model. *J. Atmos. Sci.*, **53**, 1781–1797, doi:[10.1175/1520-0469\(1996\)053<1781:TQLEOA>2.0.CO;2](https://doi.org/10.1175/1520-0469(1996)053<1781:TQLEOA>2.0.CO;2).
- Dritchel, D. G. and M. E. McIntyre, 2008: Multiple jets as PV staircases: the Phillips effect and the resilience of eddy-transport barriers. *J. Atmos. Sci.*, **65**, 855–874, doi:[10.1175/2007JAS2227.1](https://doi.org/10.1175/2007JAS2227.1).
- Farrell, B. F. and P. J. Ioannou, 1993: Stochastic dynamics of baroclinic waves. *J. Atmos. Sci.*, **50**, 4044–4057, doi:[10.1175/1520-0469\(1993\)050<4044:SDOBW>2.0.CO;2](https://doi.org/10.1175/1520-0469(1993)050<4044:SDOBW>2.0.CO;2).
- Farrell, B. F. and P. J. Ioannou, 1994: A theory for the statistical equilibrium energy spectrum and heat flux produced by transient baroclinic waves. *J. Atmos. Sci.*, **51**, 2685–2698, doi:[10.1175/1520-0469\(1994\)051<2685:ATFTSE>2.0.CO;2](https://doi.org/10.1175/1520-0469(1994)051<2685:ATFTSE>2.0.CO;2).
- Farrell, B. F. and P. J. Ioannou, 1995: Stochastic dynamics of the midlatitude atmospheric jet. *J. Atmos. Sci.*, **52**, 1642–1656, doi:[10.1175/1520-0469\(1995\)052<1642:SDOTMA>2.0.CO;2](https://doi.org/10.1175/1520-0469(1995)052<1642:SDOTMA>2.0.CO;2).
- Farrell, B. F. and P. J. Ioannou, 1996: Generalized stability. Part I: Autonomous operators. *J. Atmos. Sci.*, **53**, 2025–2040, doi:[10.1175/1520-0469\(1996\)053<2025:GSTPIA>2.0.CO;2](https://doi.org/10.1175/1520-0469(1996)053<2025:GSTPIA>2.0.CO;2).
- Farrell, B. F. and P. J. Ioannou, 2002: Perturbation growth and structure in uncertain flows. Part II. *J. Atmos. Sci.*, **59** (18), 2647–2664, doi:[10.1175/1520-0469\(2002\)059<2647:PGASIU>2.0.CO;2](https://doi.org/10.1175/1520-0469(2002)059<2647:PGASIU>2.0.CO;2).

- Farrell, B. F. and P. J. Ioannou, 2003: Structural stability of turbulent jets. *J. Atmos. Sci.*, **60**, 2101–2118, doi:[10.1175/1520-0469\(2003\)060<2101:SSOTJ>2.0.CO;2](https://doi.org/10.1175/1520-0469(2003)060<2101:SSOTJ>2.0.CO;2).
- Farrell, B. F. and P. J. Ioannou, 2007: Structure and spacing of jets in barotropic turbulence. *J. Atmos. Sci.*, **64**, 3652–3665, doi:[10.1175/JAS4016.1](https://doi.org/10.1175/JAS4016.1).
- Farrell, B. F. and P. J. Ioannou, 2008: Formation of jets by baroclinic turbulence. *J. Atmos. Sci.*, **65**, 3353–3375, doi:[10.1175/2008JAS2611.1](https://doi.org/10.1175/2008JAS2611.1).
- Farrell, B. F. and P. J. Ioannou, 2009: A theory of baroclinic turbulence. *J. Atmos. Sci.*, **66**, 2444–2454, doi:[10.1175/2009JAS2989.1](https://doi.org/10.1175/2009JAS2989.1).
- Fjørtoft, R., 1953: On the changes in the spectral distribution of kinetic energy for twodimensional, non-divergent flow. *Tellus*, **5**, 120–140, doi:[10.1111/j.2153-3490.1953.tb01051.x](https://doi.org/10.1111/j.2153-3490.1953.tb01051.x).
- Gill, A. E., 1974: The stability on planetary waves on an infinite beta-plane. *Geophys. Astrophys. Fluid Dyn.*, **6**, 29–47, doi:[10.1080/03091927409365786](https://doi.org/10.1080/03091927409365786).
- Legras, B. and M. Ghil, 1985: Persistent anomalies, blocking and variations in atmospheric predictability. *J. Atmos. Sci.*, **42**, 433–471, doi:[10.1175/1520-0469\(1985\)042<0433:PABAVI>2.0.CO;2](https://doi.org/10.1175/1520-0469(1985)042<0433:PABAVI>2.0.CO;2).
- Lilly, D. K., 1969: Numerical simulation of two-dimensional turbulence. *Phys. Fluids*, **12**, II240–II249, doi:[10.1063/1.1692444](https://doi.org/10.1063/1.1692444).
- Marston, J. B., 2012: Atmospheres as nonequilibrium condensed matter. *Annu. Rev. Condens. Matter Phys.*, **3**, 285–310, doi:[10.1146/annurev-conmatphys-020911-125114](https://doi.org/10.1146/annurev-conmatphys-020911-125114).
- Marston, J. B., E. Conover, and T. Schneider, 2008: Statistics of an unstable barotropic jet from a cumulant expansion. *J. Atmos. Sci.*, **65**, 1955–1966, doi:[10.1175/2007JAS2510.1](https://doi.org/10.1175/2007JAS2510.1).
- Miller, J., 1990: Statistical mechanics of Euler equations in two dimensions. *Phys. Rev. Lett.*, **65**, 2137–2140, doi:[10.1103/PhysRevLett.65.2137](https://doi.org/10.1103/PhysRevLett.65.2137).
- O’Gorman, P. A. and T. Schneider, 2007: Recovery of atmospheric flow statistics in a general circulation model without nonlinear eddy-eddy interactions. *Geophys. Res. Lett.*, **34**, L22 801, doi:[10.1029/2007GL031779](https://doi.org/10.1029/2007GL031779).
- Parker, J. B. and J. A. Krommes, 2013: Zonal flow as pattern formation: Merging jets and the ultimate jet length scale. *Phys. Rev. Lett.*, (sub judice, [arXiv: 1301.5059](https://arxiv.org/abs/1301.5059)).
- Rhines, P. B., 1975: Waves and turbulence on a beta-plane. *J. Fluid Mech.*, **69**, 417–433, doi:[10.1017/S0022112075001504](https://doi.org/10.1017/S0022112075001504).
- Robert, R. and J. Sommeria, 1991: Statistical equilibrium states for two-dimensional flows. *J. Fluid Mech.*, **229**, 291–310, doi:[10.1017/S0022112091003038](https://doi.org/10.1017/S0022112091003038).
- Schoeberl, M. R. and R. S. Lindzen, 1984: A numerical simulation of barotropic instability. Part I: Wave-mean flow interaction. *J. Atmos. Sci.*, **41** (8), 1368–1379, doi:[10.1175/1520-0469\(1984\)041<1368:ANSOBI>2.0.CO;2](https://doi.org/10.1175/1520-0469(1984)041<1368:ANSOBI>2.0.CO;2).
- Srinivasan, K. and W. R. Young, 2012: Zonostrophic instability. *J. Atmos. Sci.*, **69** (5), 1633–1656, doi:[10.1175/JAS-D-11-0200.1](https://doi.org/10.1175/JAS-D-11-0200.1).
- Sukoriansky, S., N. Dikovskaya, and B. Galperin, 2008: Non-linear waves in zonostrophic turbulence. *Phys. Rev. Lett.*, **101** (1), 178 501, doi:[10.1103/PhysRevLett.101.178501](https://doi.org/10.1103/PhysRevLett.101.178501).
- Tobias, S. M. and J. B. Marston, 2013: Direct statistical simulation of out-of-equilibrium jets. *Phys. Rev. Lett.*, (to appear, [arXiv:1209.3862](https://arxiv.org/abs/1209.3862)).
- Vallis, G. K. and M. E. Maltrud, 1993: Generation of mean flows and jets on a beta plane and over topography. *J. Phys. Oceanogr.*, **23**, 1346–1362, doi:[10.1175/1520-0485\(1993\)023<1346:GOMFAJ>2.0.CO;2](https://doi.org/10.1175/1520-0485(1993)023<1346:GOMFAJ>2.0.CO;2).
- Vasavada, A. R. and A. P. Showman, 2005: Jovian atmospheric dynamics: an update after *Galileo* and *Cassini*. *Rep. Prog. Phys.*, **68**, 1935–1996, doi:[10.1088/0034-4885/68/8/R06](https://doi.org/10.1088/0034-4885/68/8/R06).
- Williams, G. P., 1978: Planetary circulations: 1. Barotropic representation of Jovian and terrestrial turbulence. *J. Atmos. Sci.*, **35**, 1399–1426, doi:[10.1175/1520-0469\(1978\)035<1399:PCBROJ>2.0.CO;2](https://doi.org/10.1175/1520-0469(1978)035<1399:PCBROJ>2.0.CO;2).
- Wunsch, C., 2003: Greenland-Antarctic phase relations and millennial time-scale climate fluctuations in the Greenland ice-cores. *Quaternary Science Reviews*, **22**, 1631–1646, doi:[10.1016/S0277-3791\(03\)00152-5](https://doi.org/10.1016/S0277-3791(03)00152-5).
- Zhang, Y. and I. M. Held, 1999: A linear stochastic model of a GCM’s midlatitude storm tracks. *J. Atmos. Sci.*, **56**, 3416–3435, doi:[10.1175/1520-0469\(1999\)056<3416:ALSMOA>2.0.CO;2](https://doi.org/10.1175/1520-0469(1999)056<3416:ALSMOA>2.0.CO;2).